Tribology International 165 (2022) 107245

Contents lists available at ScienceDirect

Tribology International

journal homepage: www.elsevier.com/locate/triboint

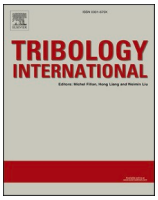

Aspects of modeling and numerical simulation of dry point contacts between viscoelastic solids

Yan Zhao [a,*], G.E. Morales-Espejel [b], C.H. Venner [a]

[a] Faculty of Engineering Technology, University of Twente, 7500AE Enschede, the Netherlands
[b] SKF Research and Technology Development, Meidoornkade 14, 3922AE Houten, the Netherlands

ARTICLE INFO

Keywords:
Contact mechanics
Viscoelasticity
Lubrication modelling
Multi-level multi-integration method (MLMI)

ABSTRACT

The virtual absence of pressure driven flow inside an elastohydrodynamic lubrication (EHL) contact leads to remarkable similarity between lubricated film thickness and separation by a viscoelastic layer as is suggested by experimental and theoretical results, see [1]. This offers interesting opportunities for mixed lubrication modeling without needing the flow continuity-based Reynolds equation. In this paper numerical simulation of viscoelastic concentrated contact modeling is revisited, first considering the problem of a viscoelastic half-space and a rigid sphere, both in static (squeeze) as well as (frictionless) rolling/sliding conditions. In particular modeling aspects are discussed so that the efficiency of computation of the viscoelastic deformation remains close to the efficiency of computation of an elastic deformation. This is achieved by rewriting Hunter's [2] deformation equation from an integral form into a differential form by applying the Leibnitz integral theorem, even for complex materials with multiple relaxation times to represent complex viscoelastic properties of materials. The approach can be straightforwardly implemented in any (EHL) contact solver regardless of the numerical method. Detailed results are presented, such as the effect of the Deborah number, the relation between the extreme cases of the rolling problem and the static problem, and discussed in detail. In addition to the rigid sphere against a viscoelastic half-space, also the case of two viscoelastic bodies is considered.

1. Introduction

Current technologies are pushed to their limits by increasingly strict efficiency demands, required reduction of material use, and required reduction of environmental impact, e.g. noise and pollution. The process towards a more sustainable society is a major challenge socio-economically, politically, as well as technically. With a major fraction of the global energy usage originating from tribological contacts to overcome friction and to remanufacture worn parts [3], innovations and improvements of lubrication technology play an essential role towards more sustainable technology. In general trends lubricated contacts are towards increasingly severe operating conditions of higher loads, reduced lubricant supply, and higher temperatures, which all lead to thinner films. In these circumstances small scale effects such as roughness moving through the contact or the particular crystallographic structure or composition/topology of the material may play an important role for lubricant film formation and contact fatigue life. In particular cases contacts will be operating close to, or even in the mixed lubrication regime. In this respect it is important to note that a paradigm shift is taking place in the field of material science, as a result of which material(s) can increasingly be designed, optimized and realized on a very local scale by new additive technologies. These developments call for advanced modeling and computational methods to be able to achieve a reliable degree of predictibility for actual design.

Regarding the lubricant film (flow) prediction most models rely on the continuum based Reynolds equation, possibly augmented with a complementarity condition to account for starvation [4] and/or a pragmatic incorporation of a minimum film threshold to allow local film breakdown in modeling mixed lubrication. However, by definition a continuum Reynolds based model is quite limited in the possibilities to model complex intermittent contact problems as well as possible variation of the rheological behaviour. Some first steps towards an alternative approach of EHL contact modeling were pioneered by van Emden et al. [1]. They argued that as the lubricant inside highly loaded contacts hardly exhibits any pressure driven flow because of the smallness of the film thickness and/or the piezoviscosity of the lubricants. It will behave much as a viscoelastic near solid layer rather than as a fluid. They thus investigated the possibility to model elastohydrodynamic lubrication (EHL) in the thin film regime, using a dry contact separated by a

* Corresponding author.
E-mail address: y.zhao-7@utwente.nl (Y. Zhao).

https://doi.org/10.1016/j.triboint.2021.107245
Received 9 June 2021; Received in revised form 18 August 2021; Accepted 19 August 2021
Available online 6 September 2021

Nomenclature

Notation

a_0	Radius of Hertzian contact with effective modulus E_f, [m] $a_0 = (\frac{3W_0R_0(1-\nu^2)}{4E_f})^{1/3}$
a	Contact radius, [m]
$\overline{a}$	Dimensionless contact radius, $\overline{a} = a/a_0$, [-]
$\overline{a}_{max}$	Dimensionless maximum contact radius, $\overline{a}_{max} = a_{max}/a_0$, [-]
E_f, E_s	Modulus of the linear springs in the SLS model, [Pa]
E_0	Effective modulus of the two springs in SLS model in series, [Pa] $1/E_0 = 1/E_f + 1/E_s$
F_r	Friction force, [N]
$\overline{F_r}$	Dimensionless friction force, $\overline{F_r} = F_r/\frac{3Wa_0}{2\pi R_0}$, [-]
h	Gap height, [m]
h_0	Penetration displacement for an undeformed contact, [m]
H	Dimensionless gap height, $H = h/\delta$, [-]
N_t	Number of time steps in time domain, [-]
p	Pressure, [Pa]
P	Dimensionless pressure, $P = p/p_H$, [-]
P_{cen}	Dimensionless central pressure, $P_{cen} = p_{cen}/p_H$, [-]
p_H	Maximum Hertzian pressure, $p_H = \frac{3W_0}{2\pi a_0^2}$, [Pa]
R_0	Radius of sphere, [m]
R_e	Elasticity ratio, $R_e = E_f/E_s$, [-]
t	Time, [s]
T	Dimensionless time, $T = t/\tau$, [-]
u	Viscoelastic deformation, [m]
u_e	Elastic deformation, [m]
U	Dimensionless viscoelastic deformation, $U = u/\delta$, [-]
V_x	Rolling velocity, [m/s]
W_0	Normal load, [N]
x, y	Coordinate, [m]
X, Y	Dimensionless coordinate, $X = x/a_0$, $Y = y/a_0$, [-]
η_s	Viscosity of the dashpot in the SLS model, [Pa · s]
τ	Relaxation time of viscoelastic material, $\tau = \eta_s/E_s$, [s]
ν	Poisson ratio, [-]
μ	Friction coefficient, $\mu = F_r/W_0$, [-]
$\overline{\tau}$	Deborah number (dimensionless velocity), $\overline{\tau} = \tau/\frac{a_0}{V_x}$, [-]
φ_c	Creep compliance operator of viscoelastic material, [-]
ψ_r	Relaxation operator of viscoelastic material, [-]
δ	Maximum Hertzian displacement, $\delta = a_0^2/R_0$, [m]
Δ_t	Uniform time step, [s]
Δ_x	Uniform mesh size in x direction, [m]

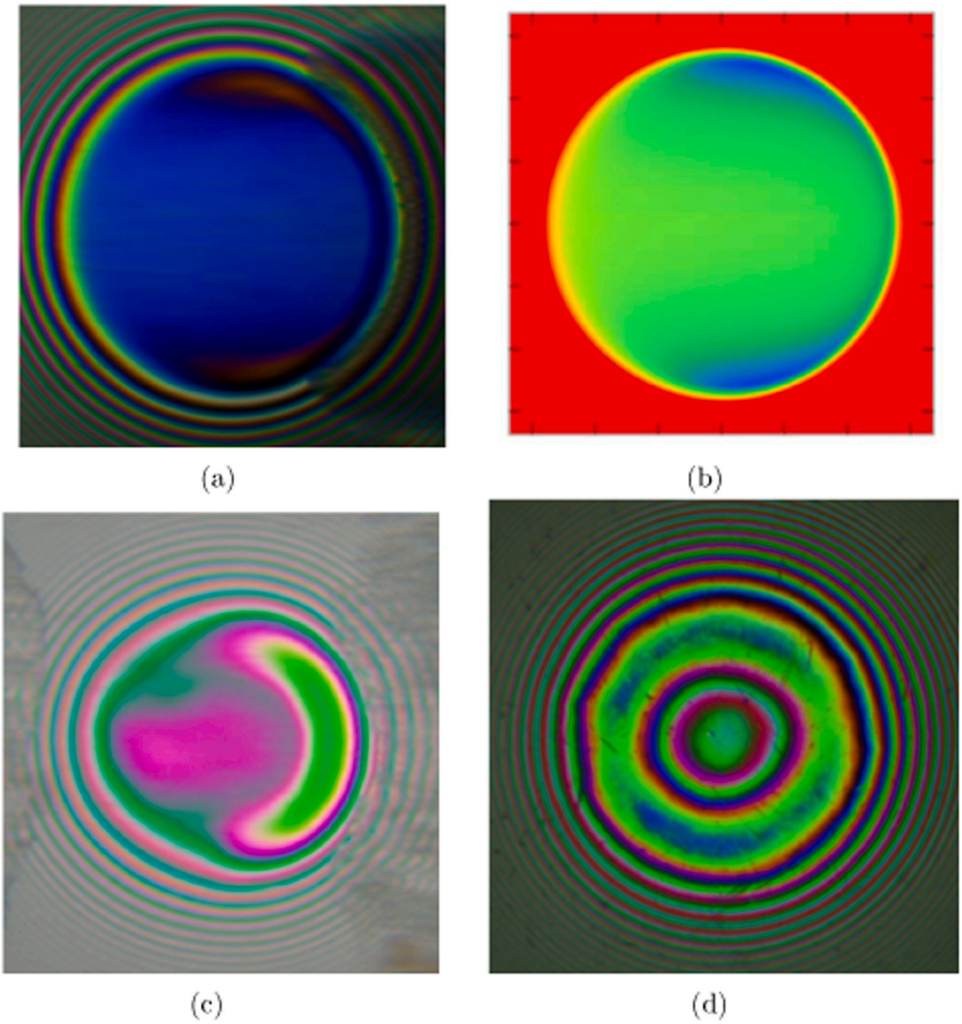

Fig. 1. Concept of viscoelastic layer lubrication and interferograms of lubricating film in concentrated point contacts between a loaded steel ball and a glass disc. (a) experimental result: a typical horse-shoe shaped EHL film measured with oil lubrication, at pure rolling; (b) simulation results with viscoelastic layer model [1], based on dry contact; (c) experimental result: PDMS viscoelastic layer lubrication, no oil, at pure rolling; (d) experimental result: indentation of PDMS viscoelastic layer with an initial thickness of 20 μm, no oil.

viscoelastic layer with a very local support. This approach yielded very interesting results.

It was demonstrated that with the dry-contact viscoelastic (oedometric) layer model, simulation results of the shape of separating film could be obtained that were strikingly similar to the well-known fully flooded fluid EHL film results obtained without solving the Reynolds equation, see Fig. 1 (a) and (b). Recently, the authors carried out experiments with a solid thin PDMS layer between a steel ball and a glass disc under pure rolling and squeeze (creep) test conditions. The film profile (shape of the deformed PDMS layer) in the contact zone was measured by optical interferometry. It is interesting to see that essential elements of fluid film lubrication, e.g. the occurrence of the characteristic side lobes during a pure rolling test and the dimple during a squeeze (creep) test, were well represented by the viscoelastic layer, see Fig. 1 (c) and (d). Note that there was no liquid lubricant except for the viscoelastic solid-like PDMS layer.

These results provide additional motivation to the possibilities to model a lubricant film as a possibly partitioned viscoelastic layer with specific local properties which can be modeled without the need of the continuum based Reynolds equation and would allow a much larger variety of constitutive behaviour to be implemented. Viscoelastic layer dry or fully flooded lubricated contacts are of interest for many applications in e.g. gels, soft matter, biomedical implants and smart devices [5–8]. As a prelude to viscoelastic layer modeling, this paper revisits modeling and numerical simulation aspects of viscoelastic behaviour for concentrated contacts under rolling as well as creep/squeeze conditions.

Viscoelastic materials, e.g. polymers and polymer-based composites, are widely used in modern engineering and biomedical fields due to their outstanding performance such as low cost, ease of manufacture, corrosion resistance and lightweight. Their physical-mechanical properties are time dependent, which cannot be treated mathematically by the laws of either solids or fluids. There can be a significant time-delayed response in a deformation process showing creep behavior. Taking static viscoelastic contact problem as an example, the prediction of contact parameters (e.g. the size of the contact zone and the pressure distribution inside the zone) based on the Hertzian theory is no longer accurate, because the response to external load depends explicitly on the viscoelastic property of the material (Section 2.2) and the loading time/history.

Modeling of linear viscoelastic material behavior is often based on the so-called correspondence principle proposed by Alfrey [9] in 1944, in which the solution to a viscoelastic problem was derived from the corresponding elastic solution in a Laplace or Fourier transformed domain [10]. The solution of static contact problems of viscoelastic materials dates back to the 1950s [9,11,12]. Lee and Radok [13] applied the correspondence principle and derived an analytical solution to the contact problem between a spherical indenter and a linear viscoelastic half-space. They proposed a generalized method to solve viscoelastic contact problems by replacing the elastic compliance in an elastic solution by a time-dependent viscoelastic creep function. However, the solution fails for the unloading process because negative pressures would appear with a decreasing contact radius. Several approaches [14–17,18] have been proposed to overcome this issue. Most studies are limited to idealized viscoelastic material with a single relaxation time. However, recently, Chen et al [19] summarized Lee and Radok's method and presented a three-dimensional (3D) semi-analytical solution which is capable to simulate the creep behavior of a viscoelastic material with multi-relaxation times coupled with Fast Fourier Transform (FFT) based algorithms. Koumi and Nelias et al. [20] extended this semi-analytical solution to contact problems between a rigid indenter and a heterogeneous viscoelastic material also using FFT based numerical methods.

Dynamic contact problems between viscoelastic bodies, including frictionless rolling and sliding motion, have been studied extensively. Hunter [2] and Goriacheva [21] proposed analytical solutions for the 2D contact problems between a rigid cylinder and a viscoelastic half-space. Panek and Kalker [22] extended Hunter's 2D line model [2] to a non-trivial 3D point contact case by enforcing the line integral approximation. Hooke and Huang [23] investigated a lubricated 2D EHL line contact problem between bodies of linear viscoelastic materials, and analyzed the influence of the viscoelastic material behaviour on the EHL film thickness and pressure. Aleksandorv et al [24] presented numerical solutions for a 3D sliding problem between a smooth sphere and a viscoelastic half-space. The above analyses are limited to ideal viscoelastic materials with one relaxation time. However, a real viscoelastic material presents a wide spectrum of relaxation times, and a single relaxation time is insufficient to represent the phenomenological viscoelastic behavior. For this purpose, viscoelastic models considering multi-relaxation times have been proposed [25–28,29]. In 2010, Persson [25] presented a new approach to estimate the apparent friction coefficient for the rolling contact of a rigid cylinder or a sphere on a viscoelastic solid. More recently, Carbone and Putignano [26] developed a novel model, which was validated through experiments later [30], to investigate rolling/sliding contact problems between viscoelastic bodies in steady-state regime using Boundary Element Method. Based on the model proposed in [26], Putignano and Dini [28,29] further investigated the influence of solid viscoelastic rheology on a lubricated contact of soft materials. Koumi et al [27] introduced elastic inhomogeneties in a viscoelastic substrate and solved the frictionless rolling contact problem using FFT methods based on the model in [19].

In principle, both the static and the dynamic contact problems of linear viscoelastic materials can be solved based on the well-established elastic deformation equation, i.e. the Boussinesq deformation equation for an elastic half-space. For the former, a time integral should be added to the elastic Boussinesq equation after applying the time integral operation according to the Boltzmann superposition principle (Appendix B). For dynamic contact problems, a simplified treatment is used to represent the time-dependent deformation equation of viscoelastic materials in a moving coordinate [20,23,26] so that the deformation can be converted into an influence coefficient in the Boussinesq elastic deformation equation [2,26]. In this way, the viscoelastic deformation in a rolling/sliding contact can also be obtained based on existing elastic deformation solutions. However, the challenging is that solving a viscoelastic contact problem is more demanding in computational time. In the literature of EHL study, it has been reported that the elastic deformation or the double integral in the Boussinesq equation can be solved efficiently by numerical methods such as discrete convolution and fast Fourier transform (DC-FFT) method [31,32] and multilevel multi-integration (MLMI) method [33,34]. In viscoelastic contact mechanics, while FFT related methods have been widely used in deformation calculation, MLMI and multigrid techniques have been rarely reported.

In this work, multigrid and MLMI methods [34] have been used to analyze dry contact problems of a viscoelastic half-space at both static and dynamic contact conditions. The standard linear solid (SLS) model, either with a single relaxation time or with multi-relaxation times, is used to characterize the viscoelastic property of the half-space. A detailed description is given on how to introduce the effect of viscoelasticity into an existing elastic solution for the numerical solution of linear viscoelastic contact problems. Firstly, for static contacts, a new expression of deformation equation was proposed which can be further used to derive the deformation equation for dynamic rolling/sliding contacts in the spatial domain. Secondly, for solving dynamic viscoelastic contact problems, a novel and efficient numerical approach is proposed allowing the considerations of multi-relaxation times while keeping almost the same computational time as that for an elastic solution. The validation of the developed model and multigrid solver is carried out by comparing the numerical results with Lee and Radok's [13] analytical solution and Carbone's [26] numerical results. After validation, the proposed model is applied to investigate the influence of types of motion, i.e. rolling and sliding, on the pressure distribution and on the contact footprint of viscoelastic materials. The correlation between the static contact problem and the dynamic contact problem at

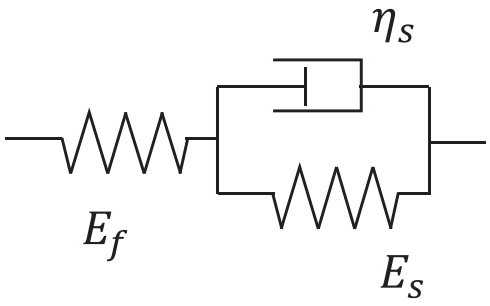

Fig. 2. Schematic of the standard linear solid viscoelastic model in the Kelvin representation.

extreme velocity conditions is pointed out.

Papers regarding viscoelastic modeling use different models and equations and the information are quite scattered in the literature. Therefore, as a prelude to viscoelastic layer modeling, this paper revisits modeling and numerical simulation aspects of viscoelastic behaviour for modeling and simulation of concentrated contacts, i.e. contact problems between a sphere and a viscoelastic half-space of single relaxation time and of multi-relaxation times at both static and frictionless dynamic rolling/sliding conditions.

2. Viscoelastic modeling

2.1. Fundamentals of viscoelasticity

Similar to the definition of the elastic modulus and the compliance in the theory of linear elasticity, two functions are defined to characterize the response of viscoelastic materials, see [8,35]. These are the creep compliance function:

$$\varphi_c(t) = \frac{\epsilon(t)}{\sigma_0} \tag{1}$$

which characterizes the strain response to a constant stress $\epsilon(t) = \varphi_c(t)\sigma_0$, and the relaxation modulus function:

$$\psi_r(t) = \frac{\sigma(t)}{\epsilon_0} \tag{2}$$

which describes the stress response to a constant strain $\sigma(t) = \psi_r(t)\epsilon_0$. The response to a time dependent stress or strain variation can be obtained from the Boltzmann superposition principle [10] for linear viscoelastic materials. The time-varying strain or stress input is decomposed in incrementally small steps, and exploiting the linearity , one obtains:

$$\sigma(t) = \epsilon_0\psi_r(t) + \int_{0^+}^{t} \psi_r(t-q)\frac{d\epsilon(q)}{dq}dq \tag{3}$$

for the stress response; and

$$\epsilon(t) = \sigma_0\varphi_c(t) + \int_{0^+}^{t} \varphi_c(t-q)\frac{d\sigma(q)}{dq}dq \tag{4}$$

for the strain response (see Appendix A for the derivation). Note that, Eqs. (3) - (4) describe how the current state of stress and strain of a viscolelastic material is the result of the entire history, including the discontinuity of application of the stress or strain.

2.2. Viscoelastic models

Linear viscoelastic material models contain two basic elements: a linear elastic spring element, and a linear Newtonian dashpot to describe viscous behavior. A material model consists of one or more units, with each unit consisting of combinations of two or more of the elementary elements in parallel, or in series. The most basic viscoelastic models consist of two elements only: the Maxwell model consists of a spring and a dashpot in series, and the Kelvin-Voigt model of a spring and a dashpot in parallel. For simple viscoelastic models as these the derivation of the creep compliance function can easily be done by solving an ordinary differential equation. Details are given in Appendix B. For more complex linear viscoelastic models, the creep compliance function can be obtained from combining the creep compliance function of the individual units, exploiting the linearity. It is emphasized that the numerical methods developed in this study can be applied to any linear viscoelastic model.

2.2.1. The Standard Linear Solid model

In this study, the three element Standard Linear Solid (SLS) model, see Fig. 2, and its multi-branch generalized version are used, described in this, and in the next section. The SLS model consists of two units in series. The first unit is a linear spring of rigidity, E_f. The second unit is a Kelvin-Voigt model consisting of a spring E_s, in parallel with a dashpot characterized by viscosity η_s.

The creep compliance function can be obtained from the creep compliance functions of the units. For the SLS model shown in Fig. 2, the units (subscript 1 and 2) are the spring and the Kelvin-Voigt model. As they are in series by definition:

$$\sigma = \sigma_1 = \sigma_2 \tag{5}$$

and

$$\epsilon = \epsilon_1 + \epsilon_2 \tag{6}$$

For the Kelvin-Voigt unit in the SLS model, we have $\sigma = \sigma_2 = E_s\epsilon_2 + \eta_s\dot{\epsilon_2}$. Using $\epsilon_1 = \frac{\sigma_1}{E_f} = \frac{\sigma}{E_f}$ and $\epsilon_2 = \epsilon - \epsilon_1$, we find

$$\sigma = E_s(\epsilon - \frac{\sigma}{E_f}) + \eta_s(\dot{\epsilon} - \frac{\dot{\sigma}}{E_f}) \tag{7}$$

as the differential equation which relates stress and strain. Written in standard form, the constitutive equation of the SLS model is:

$$E_f[\epsilon(t) + \tau\frac{d\epsilon(t)}{dt}] = (1 + R_e)\sigma(t) + \tau\frac{d\sigma}{dt} \tag{8}$$

The creep compliance function can now be derived by solving the differential equation for a constant stress input. However, it can more easily be obtained from summing up (the two units are in series) the creep compliance functions of the spring:

$$\epsilon_1(t) = \varphi_{c,1}(t)\sigma_0 = \frac{\sigma_0}{E_f} \tag{9}$$

and of the Kelvin-Voigt model. See Eq. (A17), with $E = E_s$:

$$\epsilon_2(t) = \varphi_{c,2}(t)\sigma_0 = \frac{\sigma_0}{E_s}(1 - e^{-t/}\frac{\eta_s}{E_s}) \tag{10}$$

giving:

$$\varphi_c(t) = \varphi_{c,1}(t) + \varphi_{c,2}(t) = \frac{1}{E_f}[1 + R_e(1 - e^{\frac{t}{\tau}})] \tag{11}$$

where τ is the constant (single) relaxation time $\tau = \eta_s/E_s$, and R_e is the elasticity ratio $R_e = E_f/E_s$.

2.2.2. Multi-branch SLS model

Even though the SLS model with a single relaxation time exhibits the generic aspects of viscoelastic material behavior, it will not accurately cover viscoelastic behavior of specific real materials which can exhibit a spectrum of relaxation times [8,10,26] over the length of the contact, since the material properties of both the film and the solids may spatially vary. Multiple relaxation times can be modelled by constructing a model

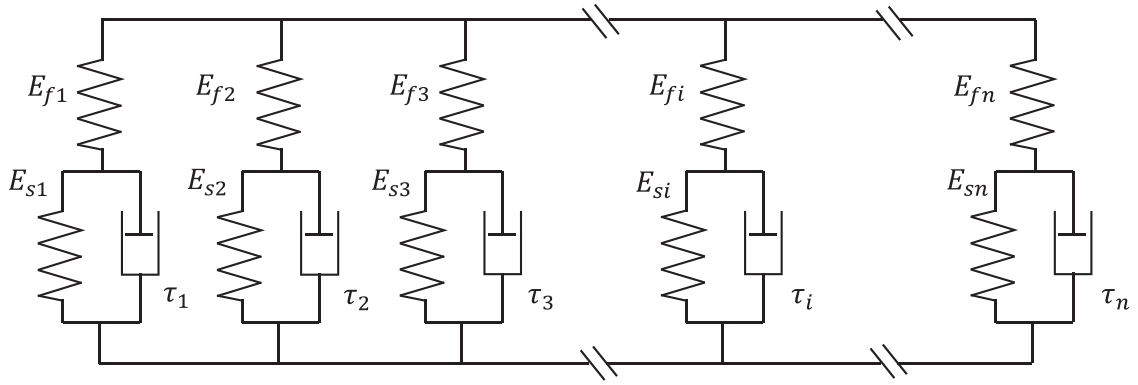

Fig. 3. Schematic of the multi-branch generalized SLS model describing viscoelastic behaviour with multiple relaxation times.

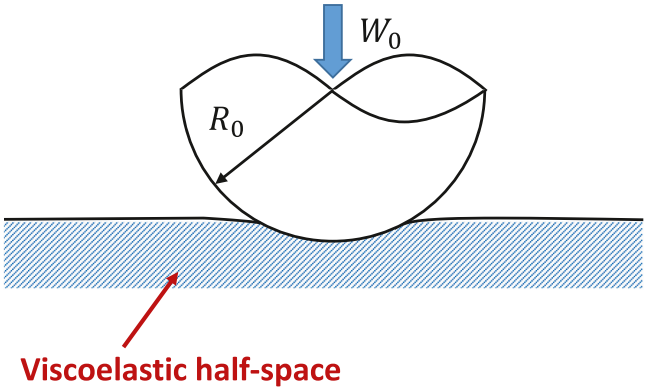

Fig. 4. Static viscoelastic contact formed between a rigid spherical indenter and a viscoelastic half-space with a applied constant normal load.

in which each of the units is a SLS model by itself, see Fig. 2, and the units are in parallel, see Fig. 3. This is referred to as the multi-branch generalized SLS model.

In this case, the unit-directional constitutive relations form a set of n equations, where n is the number of branches considered.

$$\begin{cases} E_{f1}\left[\epsilon(t)+\tau_1\dfrac{d\epsilon(t)}{dt}\right]=(1+R_{e1})\sigma_1(t)+\tau_1\dfrac{d\sigma_1}{dt} \\ E_{f2}\left[\epsilon(t)+\tau_1\dfrac{d\epsilon(t)}{dt}\right]=(1+R_{e2})\sigma_2(t)+\tau_2\dfrac{d\sigma_2}{dt} \\ \quad\cdots \\ E_{fn}\left[\epsilon(t)+\tau_n\dfrac{d\epsilon(t)}{dt}\right]=(1+R_{en})\sigma_n(t)+\tau_n\dfrac{d\sigma_n}{dt} \end{cases} \tag{12}$$

where $\tau_i=\eta_{si}/E_{si}$ and $R_{ei}=E_{fi}/E_{si}$. The closure relation of the system is the expression that the overall stress equals the sum of the stresses in the branches (units):

$$\sigma=\sum_{i=1}^{n}\sigma_i(t) \tag{13}$$

2.3. Viscoelastic dry contact equations

Concentrated point contact problems are considered under both static (zero speed) and rolling (and frictionless sliding) condition involving viscoelastic materials. The governing equations, in particular the viscoelastic deformation modeling equations, are presented below.

2.3.1. Static contact

By static contact it is meant that the surfaces of the solids have no surface speed. The static contact problem between a rigid sphere and a viscoelastic half-space, schematically shown in Fig. 4, is firstly analyzed. A normal load W_0 is instantaneously applied to the viscoelastic half-space through a spherical indenter of radius R_0. Subsequently the load is kept constant. The objective is to obtain the variation of the local deformation, the contact region, and the pressure distribution with time.

The static dry contact problem of viscoelastic materials can be modeled, like the elastic dry contact (Hertzian) problem [34], by two equations, and a complementarity condition. The equations are the gap height equation, Eq. (14), consisting of the undeformed gap shape approximating the surfaces of the contacting elements as parabolas, and their normal deformation. Next, the load balance equation, Eq. (15), stating that, neglecting the contact dynamics, the integral over the pressure should equal the externally applied load at all times. Finally, the actual complementarity problem to be solved, is stated in Eq. (16). The gap is closed and the pressure is positive, or the gap is open, and, neglecting adhesion, the pressure is zero (ambient). This is the Hertz-Signorini-Moreau condition.

$$h(x,y,t)=h_0(t)+\frac{x^2}{2R_0}+\frac{y^2}{2R_0}+u(x,y,t) \tag{14}$$

$$W_0(t)=\iint p(x,y,t)\mathrm{d}x\mathrm{d}y \tag{15}$$

$$\begin{aligned} &h(x,y,t)=0, p(x,y,t)>0, \text{ in contact area} \\ &h(x,y,t)>0, p(x,y,t)=0, \text{ out contact area} \end{aligned} \tag{16}$$

Note that, in Eqs. (14)-(16) the variables gap height h, the pressure p, and the normal deformation u, are varying in time, due to the viscoelasticity only as the load is assumed to be constant. The normal deformation u for viscoelastic materials can be expressed as:

$$u(x,y,t)=\varphi_c(t)w_e(x,y,0)+\int_{0^+}^{t}\varphi_c(t-q)\Delta_p w_e(x,y,q)dq \tag{17}$$

where $w_e(x,y,t)=\frac{1-\nu^2}{\pi}\iint\frac{p(x',y',t)}{\sqrt{(x-x')^2+(y-y')^2}}\mathrm{d}x'\mathrm{d}y'$ is the elastic deformation integral transform with the pressure distribution as input, and

$$\Delta_p w_e(x,y,q)=\frac{1-\nu^2}{\pi}\iint\frac{1}{\sqrt{(x-x')^2+(y-y')^2}}\frac{\partial p(x',y',q)}{\partial q}\mathrm{d}x'\mathrm{d}y' \tag{18}$$

is the same integral transform but with the time derivative of the pressure as input. Eq. (17) is based on the Boussinesq solution for an elastic infinite half-space [36] and the correspondence principle [10]. The derivation is given in Appendix C. The equation is also used in [19,27]. Eq. (17) can be rewritten as:

$$u(x,y,t)=\varphi_c(0)w_e(x,y,t)+\int_{0^+}^{t}\frac{d\varphi_c(q)}{dq}w_e(x,y,t-q)dq \tag{19}$$

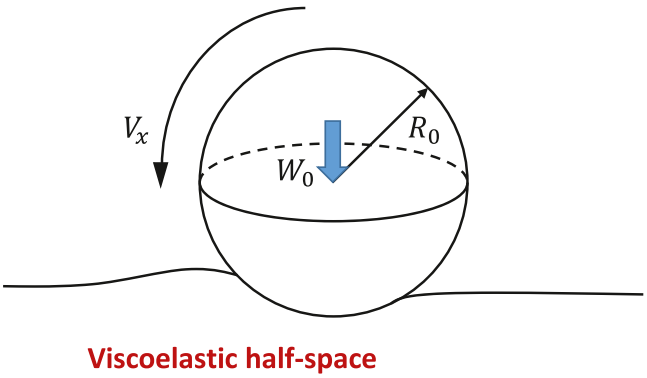

Fig. 5. Dynamic rolling viscoelastic point contact problems formed between a rigid sphere with a viscoelastic half-space.

For details of the derivation of Eq. (17) and Eq. (19), see Appendix C. Note that Eq. (19) uses the derivative of the creep compliance function, rather than the derivative of the pressure in Eq. (17) to obtain the static viscoelastic deformation. Both equations should of course lead to the same result. However, Eq. (19) has an advantage from the numerical solution point of view as, when a given solver for elastic material contact problems is available the extension to viscoelastic behaviour is rather straightforward as the computation of the time derivative of the pressure is not needed. Also, when large derivatives occur in the pressure distribution, numerical approximation via Eq. (19) may be more accurate as the derivative of the compliance function can often be determined analytically. Implementation in a numerical solver is discussed in Sec. 3.

2.3.2. *Rolling contact problem*

The second problem where the surfaces are in motion is illustrated in Fig. 5. For simplicity in the description, we restrict ourselves to a rigid sphere rolling on a stationary viscoelastic half-space with a constant surface speed V_x under a constant normal load W_0. However, the methods presented here can also be used for the case where both surfaces are moving, and for the case of two viscoelastic half-spaces. Some of these aspects will be discussed in the results of Sec. 4.

For the rolling contact, relative to the contact location the situation is steady state. The time-dependent governing equations, Eqs.(14) - (16), in the inertial coordinate system can be transformed to a reference frame fixed to the contact location. In that reference the governing equations for the dynamic contact problems are the same as Eqs. (14)–(16), see Appendix C, with the variable x, in the deformation integral for the viscoelastic body replaced by the transformed speed-dependent variable $x-V_xt$, to account for the motion of the viscoelastic material relative to the contact location. Note that when the surface is non-smooth also in the terms for the undeformed shape one needs to account for the motion relative to the contact location in this way. In the new reference frame, Eq. (19) for the deformation can be expressed as:

$$u(x,y) = \varphi_c(0)w_e(x,y) + \int_0^\infty \frac{d\varphi_c(q)}{dq} w_e(x - V_x q, y)dq \tag{20}$$

where $w_e(x - V_x q, y) = \frac{1-\nu^2}{\pi} \iint \frac{p(x',y')}{\sqrt{(x-V_x q-x')^2+(y-y')^2}} \mathrm{d}x'\,\mathrm{d}y'$. For the EHL line contact between viscoelastic bodies, Eq. (20) was also used by Hooke and Huang [23].

Finally, two approaches were used to calculate the tangential force (rolling resistance of friction) generated in the contact between a rigid sphere and viscoelastic half-space through the moment equilibrium or projecting pressure along the deformed surface.

(1) *Friction deduced from moment equilibrium*: the friction force, F_r, can be deduced by calculating the moment which prevents the sphere from rotating.

$$F_r R_0 = \iint xp(x,y)\mathrm{d}x\mathrm{d}y \tag{21}$$

(2) *Friction deduced from pressure projection*: the friction force, F_r, can also be obtained by projecting pressure along the axis ox, as shown in Fig. 6. The friction force reads:

$$F_r = \iint p(x,y)sin\alpha \mathrm{d}x\mathrm{d}y \tag{22}$$

where $tan\alpha = \frac{\partial u(x,y)}{\partial x}$. This method allows equivalent interfical shear stress representation of the friction to be defined on each point of the surface $\tau_{\text{interface}} = p(x,y)sin\alpha$. Once the rolling friction is obtained with either Eq. (21) or Eq. (22), the friction coefficient can be simply calculated with

$$\mu = \frac{F_r}{W_0} \tag{23}$$

3. Numerical Solution

To achieve numerical solutions for the two contact problems given in Sec. 2, i.e. Eqs. (14) - (16) with the viscoelastic deformation given by Eq. (17) or Eq. (19) for the static contact problem, and by Eq. (20) for rolling contact problem, must be solved. A spatial domain $x_{\text{in}} \le x \le x_{\text{out}}$ and $y_{\text{in}} \le y \le y_{\text{out}}$ is used where $x_{\text{in}} = y_{\text{in}} = -3a_0$ and $x_{\text{out}} = y_{\text{out}} = 3a_0$ is taken, with a_0 the contact radius corresponding to the instantaneous elastic response of the viscoelastic material, i.e. with the instantaneous modulus E_f of the free spring in the SLS model (Fig. 2). The resulting non-dimensional variables are:

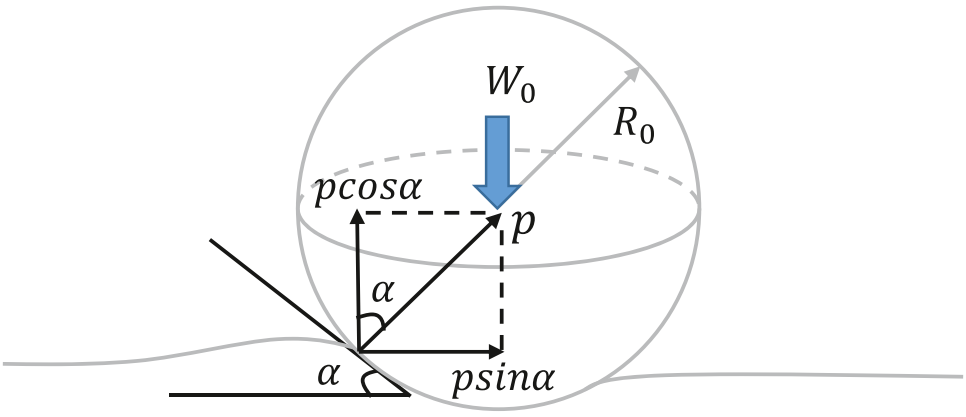

Fig. 6. Pressure projection for friction calculation.

$$a_0=\sqrt[3]{\frac{3W_0R_0(1-\nu^2)}{4E_f}},p_H=\frac{3W_0}{2\pi a_0^2},\delta=\frac{a_0^2}{R_0},\overline{t}=\frac{\tau V_x}{a_0},\overline{a}=\frac{a}{a_0},H=\frac{h}{\delta},P=\frac{p}{p_H},$$

$$U=\frac{u}{\delta},H_0=\frac{h_0}{\delta},T=\frac{t}{\tau},X=\frac{x}{a_0},Y=\frac{y}{a_0} \tag{24}$$

The domain in dimensionless space is thus $-3 \le X \le 3$ and $-3 \le Y \le 3$.

$$\Delta_p^n w_e(x,y,n\Delta_t)=\frac{1-\nu^2}{\pi}\iint\frac{1}{\sqrt{(x-x')^2+(y-y')^2}}\frac{p(x',y',n\Delta_t)-p(x',y',(n-1)\Delta_t)}{\Delta_t}\mathrm{d}x'\mathrm{d}y' \tag{27}$$

For the static surface problem a time domain, $0 \le T \le 5$, is taken and divided into $N_t = 200$ (uniform) steps in time.

Various methods exist for the discretization of the problem, e.g. finite difference and Finite Element Methods [37], for the numerical solution, e.g. conjugate gradient method [38], local iterative methods, local iterative methods using Multilevel/Multigrid techniques for convergence acceleration [34], and global iterative methods (Newton Raphson), each with their own merits. As part of solving the equation, evaluating the integral transforms is a computationally expensive task, which can be accelerated using FFT methods [31,32,39], Fast Multipole Methods [40], or MLMI methods [33,34]. For the present study the elastic (Hertzian) dry contact numerical solver published in [34] was taken as a starting point.

A second order finite difference method was used on a uniform grid for the spatial discretization of the equations. The numerical solution of the equations (at each time step) was done using a distributive relaxation process as used for the elastic dry contact problem augmented with coarser grids in a multigrid cycle to accelerate convergence to a grid independent rate [34]. The force balance equation can be treated as a global constraint in this cycle. For the fast evaluation of the spatial integral transforms in Eq. (17) or Eq. (20), MLMI method was used, see [33,34]. This serves as a good example to see the increase in computational complexity when changing an existing numerical solution algorithm from an elastic to a viscoelastic contact problem. Since the modifications are mainly related to the computation of the viscoelastic deformation, the following description focuses on these aspects.

3.1. Static contact

The discretization of the spatial integral transforms in Eq. (17) or Eq. (19) for the viscoelastic deformation was done in the same way as for the elastic contact problem [34]. Assuming a piecewise constant pressure on integration intervals e.g. of the size of a gridcell around a grid point, the deformation in each grid point can be approximated by a summation over all contributions from the integration intervals. This yields a multi-summation (full matrix multiplication) with influence coefficients that can be determined analytically [34]. The discretization is of second order as mentioned above. To account for the viscoelastic effect of the pressure history, the time integral in Eq. (17) or Eq. (19) needs to be discretized too. Assuming a uniform timestep Δ_t a first order backward (in time) discretization of the pressure derivative in Eq. (18) can be used:

$$\frac{\partial p(x',y',q)}{\partial q}=\frac{p(x',y',q)-p(x',y',q-\Delta_t)}{\Delta_t}+o(\Delta_t) \tag{25}$$

Let $u(x, y, k\Delta_t)$ and $p(x, y, k\Delta_t)$ represent the total deformation and the pressure at a location (x, y) at time $t = k\Delta_t$, with $k(0 \le k \le N_t)$ indicating the (uniform) timestep. The resulting discretization in time of Eq.(17) can then be written as:

$$u(x,y,k\Delta_t)=\varphi_c(k\Delta_t)w_e(x,y,0)+\sum_{n=1}^{k}\varphi_c((k-n)\Delta_t)\Delta_p^n w_e(x,y,n\Delta_t)\Delta_t \tag{26}$$

where $w_e(x, y, 0)$ is as defined in Eq. (17), and is the discrete equivalent in time of Eq. (18). Even though the discretization in time is strictly first order it should be noted that the derivatives in time of the compliance are generally quite smooth so that at a timestep comparable to the mesh size effectively the second order discretization error in space will dominate. Note that the evaluation of the viscoelastic deformation in time is not a one step incremental procedure. At a particular time(step) its summation of integral transforms at each previous timesteps multiplied with a creep contribution which depends on both the previous timestep(s) $(1 \ldots n)$ as well as the time (step) at which the result is required (k). This is most efficiently achieved by storing the integral transforms (Eq. (27)) at each timestep, so they can be used again at later timesteps but then multiplied e.g. with the creep function of a different time delay $(k - n)$. Assuming that the convergence is grid independent, as is achieved using Multigrid/Multilevel techniques, the total computational effort of the algorithm is then of the order of $N_t(N_t + 1)/2 * o(NlogN)$ where N is the number of points on the spatial grid, and $o(NlogN)$ the amount of work of the evaluation of the discrete spatial integral transform when done using e.g. FFT methods or Multilevel Multi-Integration.

The discretization of Eq. (19) in time can be done also by approximating the integral over time by a summation:

$$u(x,y,k\Delta_t)=\varphi_c(0)w_e(x,y,k\Delta_t)+\sum_{n=1}^{k}\frac{d\varphi_c(q)}{dq}|_{q=n\Delta_t}w_e(x,y,(k-n)\Delta_t)\Delta_t \tag{28}$$

where $w_e(x, y, t)$ is as defined in Eq. (17), the (instantaneous) 'elastic' response to the pressure, $p(x, y, n\Delta_t)$, $(0 \le n \le k)$, at time $t = n\Delta_t$, which discretized on the spatial grid gives the already explained multi-summation.

Two numerical approaches can now be used to calculate the total viscoelastic deformation at the k^{th} time step:

Numerical Method 1 (NM1) Using the derivative of pressure (Eq. (17), Eq. (26)): substitution of Eq. (11), the creep compliance function of the SLS viscoelastic model, in Eq. (26), gives:

$$u(x,y,k\Delta_t)=\frac{1}{E_f}[1+R_e(1-e^{-\frac{k\Delta_t}{\tau}})]w_e(x,y,0)+\sum_{n=1}^{k}\frac{1}{E_f}[1+R_e(1-e^{-\frac{(k-n)\Delta_t}{\tau}})]\Delta_p^n w_e(x,y,n\Delta_t)\Delta_t \tag{29}$$

Numerical Method 2 (NM2) Using the derivative of creep function (Eq. (19), Eq. (28)): substitution of Eq. (11), the creep compliance function of the SLS viscoelastic model, in Eq. (28), the following equation is obtained:

$$u(x,y,k\Delta_t)=\frac{1}{E_f}w_e(x,y,k\Delta_t)+R_e\frac{1}{E_f}\frac{1}{\tau}\sum_{n=1}^{k}e^{-\frac{n\Delta_t}{\tau}}w_e(x,y,(k-n)\Delta_t)\Delta_t \tag{30}$$

The continuous expressions for the spatial integral transfers are approximated by multi-summations, see [34] and the governing equations given in Sec. 2.3 solved using either Eq. (29) or Eq. (30) for the viscoelastic deformation. The procedure starts with the Hertzian pressure for the instantaneous elastic response of the material as initial approximation at $T = 0$. Subsequently for each timestep the equations are solved to obtain the time evolution of pressure and gap height. For the multigrid method, without additional description, 513 * 513 node points have been used on the finest level of grid (level 5). The discrete equations of each timestep were solved until the pressure distribution satisfies the load balance equation with an absolute error smaller than 10^{-4}.

3.2. Rolling contact

To determine the viscoelastic deformation in the coordinate system relative to the contact, the creep compliance function of the SLS model can be substituted in Eq. (20) giving

$$u(x,y) = u_e(x,y) + R_e\frac{1}{\tau}\int_0^\infty e^{-\frac{q}{\tau}}u_e(x - V_x q, y)dq \tag{31}$$

where $u_e(x - V_x q, y)$ in Eq. (31) is the instantaneous elastic deformation at location of $(x - V_x q, y)$:

$$u_e(x - V_x q, y) = \frac{1-\nu^2}{\pi}\frac{1}{E_f}\iint \frac{p(x',y')}{\sqrt{(x - V_x q - x')^2 + (y - y')^2}}\mathrm{d}x'\mathrm{d}y' \tag{32}$$

Substitution of the integration variable with $s = x - V_x q$ in Eq.(31) gives:

$$u(x,y) = u_e(x,y) + R_e\frac{1}{V_x\tau}\int_{-\infty}^{x} e^{\frac{s-x}{V_x\tau}}u_e(s,y)ds \tag{33}$$

The spatial domain is taken to extend over $x_{\text{in}} \le x \le x_{\text{out}}$ and $y_{\text{in}} \le y \le y_{\text{out}}$, where $x_{\text{in}} = y_{\text{in}} = -3a_0$ and $x_{\text{out}} = y_{\text{out}} = 3a_0$. Assuming that the computational domain is taken sufficiently large so that all points (s, y) are inside the domain, and that the gridpoints (s, y) with $x_{in} \le s \le x$ coincide with the meshed grid points (x, y) by setting that the $V_x\Delta t$ equals to the mesh size Δx in the x direction. The discretization of the spatial integral transform $u_e(s, y)$ and its evaluation, can be done in exactly the same way as that of $u_e(x, y)$. When evaluating the deformation at a point (x, y), the effect of the deformation at all previous points (s, y), $x_{\text{in}} \le s \le x$, on the deformation of the current point is equivalent to the result of multiplying its elastic deformation by the exponential decay function, $e^{\frac{s-x}{V_x\tau}}$, and summing up as equivalent of the continuous integration over s in Eq. (33). As the elastic deformation is evaluated for all locations on the grid simultaneously, this multiplication can easily be done. However, while this evaluation is straightforward, the resulting discrete deformation has a larger discretization error than made in the standard elastic deformation because of the division by the velocity, $dq = ds/V_x$, and gives a grid (mesh size Δx) dependent solution, see Sec. 4.2. This implies that to maintain comparable accuracy when decreasing the speed, a more dense grid should be used, at least in the velocity direction. This point is also noted by Hooke and Huang [23]. However, this problem can be overcame in a different, grid (mesh size) independent way.

Defining:

$$\Re(x,y) = \frac{1}{V_x\tau}\int_{-\infty}^{x} e^{\frac{s-x}{V_x\tau}}u_e(s,y)ds \tag{34}$$

and taking its derivative with respect to x using the Leibnitz integral theorem:

$$\frac{\partial\Re}{\partial x} = \frac{1}{V_x\tau}e^{\frac{s-x}{V_x\tau}}u_e(s,y)|_{s=x} - \left(\frac{1}{V_x\tau}\right)^2\int_{-\infty}^{x} e^{\frac{s-x}{V_x\tau}}u_e(s,y)ds \tag{35}$$

one obtains

$$V_x\tau\frac{\partial\Re}{\partial x} = u_e(x,y) - \Re \tag{36}$$

From the original definition of $\Re$ in Eq. (34), the following relation can be obtained

$$\Re(x,y) = \frac{u(x,y) - u_e(x,y)}{R_e} \tag{37}$$

Substituting of Eq.(37) in Eq. (36), one obtains a new form of the viscoelastic 'Boussinesq' equation with a single relaxation time

$$u(x,y) + V_x\tau\frac{\partial u(x,y)}{\partial x} = (1 + R_e)u_e(x,y) + V_x\tau\frac{\partial u_e(x,y)}{\partial x} \tag{38}$$

This equation can now be discretized in space, e.g. assume or simplicity the use of a first order backward scheme, $\frac{\partial u(x,y)}{\partial x} \approx \frac{u(x,y)-u(x-\Delta_x,y)}{\Delta_x}$ and $\frac{\partial u_e(x,y)}{\partial x} \approx \frac{u_e(x,y)-u_e(x-\Delta_x,y)}{\Delta_x}$. Substitution in Eq. (38) gives an equation from which $u(x, y)$ can be solved in each point for a given y, by marching in the positive x direction, with $u_e(x, y)$ known. Once the elastic contribution is known, the extra work to obtain the viscoelastic deformation is then just one pass over the grid at each point involving only a few multiplications and additions. This is a major advantage over direct simulation via Eq. (31) and also computationally cheaper and more accurate especially for low velocities as detailed in Sec. 4.2.

3.3. Multi-relaxation times

Finally, we consider the use of a more complex viscoelastic model with multiple relaxation times. The viscoelastic 'Boussinesq' equation, Eq. (38) for the SLS model with a single relaxation time, can be extended to consider multiple relaxation times using the generalized viscoelastic model shown in Fig. 3 (the parallel-connected multi-branch SLS model).

$$\left\{\begin{array}{l} u + V_x\tau_1\dfrac{\partial u}{dx} = \dfrac{(1+R_{e1})}{E_{f1}}u_{e1} + \dfrac{V_x\tau_1}{E_{f1}}\dfrac{\partial u_{e1}}{dx} \\ u + V_x\tau_2\dfrac{\partial u}{dx} = \dfrac{(1+R_{e2})}{E_{f2}}u_{e2} + \dfrac{V_x\tau_2}{E_{f2}}\dfrac{\partial u_{e2}}{dx} \\ \cdots \\ u + V_x\tau_i\dfrac{\partial u}{dx} = \dfrac{(1+R_{ei})}{E_{fi}}u_{ei} + \dfrac{V_x\tau_i}{E_{fi}}\dfrac{\partial u_{ei}}{dx} \\ \cdots \\ u + V_x\tau_n\dfrac{\partial u}{dx} = \dfrac{(1+R_{en})}{E_{fn}}u_{en} + \dfrac{V_x\tau_n}{E_{fn}}\dfrac{\partial u_{en}}{dx} \end{array}\right\} \tag{39}$$

where $u_{ei}(x,y) = \frac{1-\nu^2}{\pi}\iint\frac{p_i(x',y')}{\sqrt{(x-x')^2+(y-y')^2}}\mathrm{d}x'\mathrm{d}y'$, while the total pressure which is applied on the surface is

$$p(x,y) = \sum_i p_i(x,y) \tag{40}$$

The definition of the surface displacement in each branch calls for the calculation of a surface double integral, u_{ei}. A direct calculation is time consuming when large numbers of mesh points and relaxation times are considered. Thus, a numerical approach is proposed which allows the considerations of multi-relaxation times while keeping the same level of computational time as that for an elastic solution. The differential equation for each branch is developed using backward first order discrete operators as follows

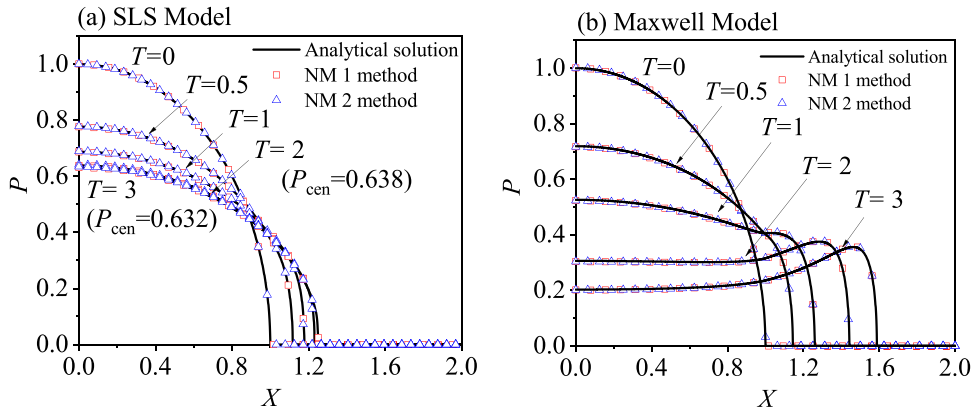

Fig. 7. Dimensionless pressure as a function of the (dimensionless) coordinate at different times during creep for a static contact problem under a instantaneously applied load: Comparison of the results of two numerical solution approximations, and the analytical solution of Lee and Radok [13]. The results are for the case of (a) SLS model with $R_e = 1$, and (b) Maxwell model.

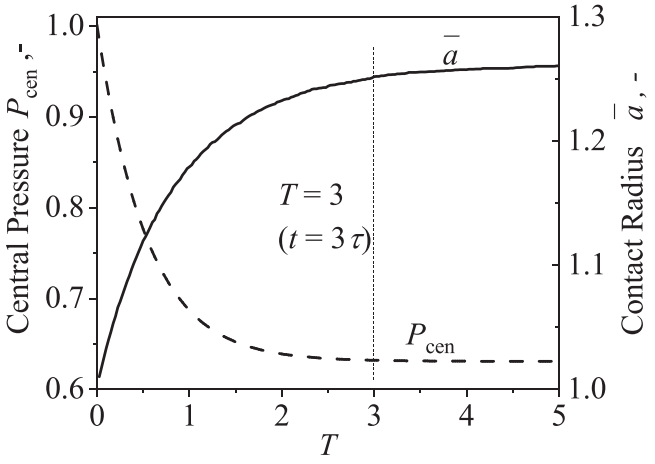

Fig. 8. Variations of the dimensionless central pressure and the contact radius with dimensionless time during the creep process. Static contact with instantaneous load (SLS viscoelastic model, $R_e = 1$, NM 2 for surface deformation).

$$\left\{\begin{array}{l} a_1 u_{l,m} - b_1 u_{l-1,m} = u_{e1l,m} - c_1 u_{e1l-1,m} \\ a_2 u_{l,m} - b_2 u_{l-1,m} = u_{e2l,m} - c_2 u_{e2l-1,m} \\ \cdots \\ a_i u_{l,m} - b_i u_{l-1,m} = u_{eil,m} - c_i u_{eil-1,m} \\ \cdots \\ a_n u_{l,m} - b_n u_{l-1,m} = u_{enl,m} - c_n u_{enl-1,m} \end{array}\right\} \tag{41}$$

The indices, l and m correspond to the position of the mesh point in the ox and oy directions. The index i indicates the branch of the model that is considered. The coefficient a_i, b_i, and c_i are defined as below

$$\begin{aligned} a_i &= \frac{1 + \dfrac{V_x \tau_i}{\Delta_x}}{\dfrac{1+R_e}{E_{fi}} + \dfrac{\dfrac{V_x \tau_i}{\Delta_x}}{E_{fi}}} \\ b_i &= \frac{\dfrac{V_x \tau_i}{\Delta_x}}{\dfrac{1+R_e}{E_{fi}} + \dfrac{\dfrac{V_x \tau_i}{\Delta_x}}{E_{fi}}} \\ c_i &= \frac{\dfrac{V_x \tau_i}{\Delta_x}}{1 + R_e + \dfrac{V_x \tau_i}{\Delta_x}} \end{aligned} \tag{42}$$

where Δ_x is the mesh size in the ox direction. Summing all the equations in Eq. (41) leads to the following relation, which enables the determination of the surface displacement

$$u_{l,m} = \frac{1}{\sum_i a_i}\left(u_{el,m} - \sum_i c_i u_{eil-1,m} + u_{l-1,m}\sum_i b_i\right) \tag{43}$$

The first term in the bracket corresponds to the 'elastic' displacement

$$u_e'(x,y) = \frac{1-\nu^2}{\pi}\iint \frac{p(x',y')}{\sqrt{(x-x')^2 + (y-y')^2}}\,\mathrm{d}x'\,\mathrm{d}y' \tag{44}$$

To obtain the surface displacement, the mesh is visited in a lexicographic order along the rolling direction. First, the elastic deformation, $u_{el,m}$, is calculated. All the other terms, $u_{eil-1,m}$ and $u_{l-1,m}$, in the bracket are known from previous calculations. Once the surface displacement, $u_{l,m}$, is calculated, the surface displacement for each individual branch can then be found using the following relation

$$u_{eil,m} = a_i u_{l,m} - b_i u_{l-1,m} + c_i u_{eil-1,m} \tag{45}$$

Only the terms calculated in the previous mesh points need to be kept in memory. The method only requires the surface displacement and the total pressure to be restored for the determination of the surface displacement whatever the number of the relaxation times are. The integral transform to be calculated is the same as the one used for an elastic problem.

4. Results and discussion

Numerical results are presented for the contact problems described before, and the different ways of evaluating the viscoelastic deformation. In Sec. 4.1, results are presented for the static contact problem computing the compliance in time subject to a fixed load. These results are validated with analytical solutions. In Sec. 4.2 results are presented for the moving contact. First for a rigid indenter rolling over a viscoelastic surface the method is verified against results published in the literature. Next, detailed results are presented showing the influence of various model parameters for a rolling contact such as the Deborah number, and the ratios of the elastic springs in the SLS model.

4.1. Static contact results

The results obtained with the two different numerical approaches are validated by comparing with the analytic solution given by Lee and Radok [13] for static contact problems under an instantaneously applied load (see in Section 2.3.1). All results are presented in dimensionless

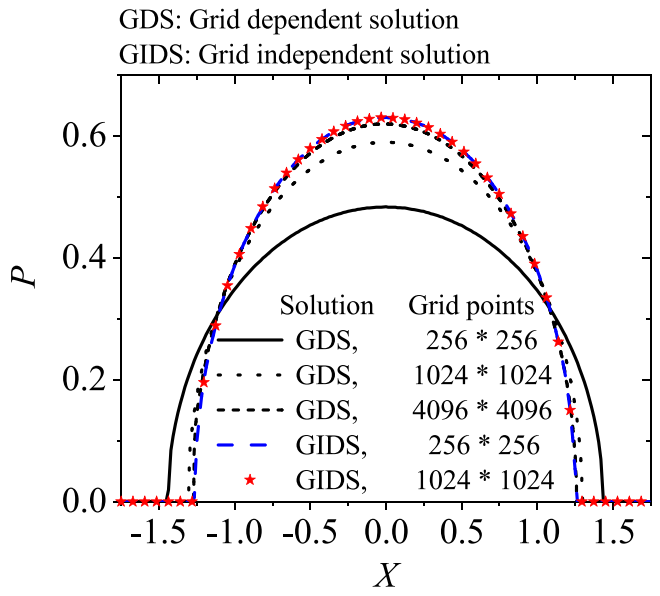

Fig. 9. The Grid Dependent Solution (GDS) and the Grid Independent Solution (GIDS) of pressure distributions along the central line of the contact with different grid points for a small rolling velocity, $\bar{\tau} = 0.01$ (SLS viscoelastic model, $R_e = 1$).

forms using the dimensionless parameters shown in Eq. (24), based on the instantaneous response of the viscoelastic half-space, the modulus E_f in the SLS model, see Fig. 2.

Fig. 7 shows the (dimensionless) pressure profile at the centerline of the contact as a function of the dimensionless coordinate X at different times relative to the relaxation time. Owing to radial symmetry only half of the profile is shown. Fig. 7 (a) shows the results for the SLS model and Fig. 7 (b) shows the results for the Maxwell model. In both figures the analytic solution is shown, as well as the results obtained using the NM1 formulation (with pressure derivative) and the NM2 formulation (with derivative of the creep function). Firstly, the numerical results show excellent agreement with the analytic solution. The excellent agreement of both computational approaches NM1 and NM2 with the analytic solution also shows the effectiveness of the newly derived viscoelastic deformation equation, Eq. (19) used in the NM2, by adopting the derivative of the creep compliance function to replace the derivative of the pressure in Eq. (17) (NM1).

Fig. 8 shows the variation of the central pressure and the contact radius with (dimensionless) time T in a creep process for the SLS viscoelastic material. Initially the material responds purely elastic to the instantaneous applied load. Only the free spring, see Fig. 2, in the SLS model responds, giving a Hertzian pressure distribution with dimensionless central pressure P_{cen} and dimensionless contact radius $\bar{a}$ of unity, because the scaling used is based on these Hertzian contact parameters. As time increases, the material creeps under the applied constant load. The contact radius $\bar{a}$ increases as the load is fixed, and with increasing contact area the central pressure P_{cen} decrease, see Fig. 8. The time rate of change of the contact radius and the maximum pressure decreases in time, which are consistent with the viscoelastic model used. As anticipated for $T \geq 3$, i.e. at a time larger than three times of the relaxation time of the material, the contact pressure and contact radius are close to their asymptotic values which are determined by the two springs in series. According to the analytical solution of Lee and Radok [13], the maximum contact radius is $\bar{a}_{\max} = (1+R_e)^{\frac{1}{3}}|_{R_e=1} = 1.2599$. In the current simulation when $T = 5$, the dimensionless radius has reached a value of 1.25, which is very close to this maximum analytical value. The maximum contact pressure is $P_{\text{cen}} = (1+R_e)^{-\frac{2}{3}}|_{R_e=1} = 0.63$. With increasing time, the numerical result approximates this value. As indicated in the figure at $t = 2\tau$ the value is observed value is 0.638, and at $t = 3\tau$ it is 0.632, see Fig. 7 (a).

Whereas the results for the SLS model in time converge to the steady Hertzian contact for the elastic modulus representative of the sum of the two springs, the results for the Maxwell model in Fig. 7 (b) show a continuous creep in time. The contact region continuously extends and the pressure lowers, as is consistent with the fact that initially both springs accommodate the load completely, after which the viscous damper relaxes the load.

4.2. Rolling contact results

To avoid the grid dependent solution with the deformation Eq. (31) as explained in Sec. 3.2, all the results shown in the following parts are obtained by solving Eq. (38). Eq. (31) gives a straightforward way to calculate the viscoelastic deformation, but there is large discretization error especially at small velocities. This can be clearly seen from Fig. 9, which shows the pressure distributions obtained by solving the Eq. (31) and Eq. (38) respectively for a small dimensionless velocity, $\bar{\tau} = 0.01$. With increasing number of grid points from 257 to 1024 in each computational direction, Eq. (31) results in a grid dependent solution (GDS) with the maximum pressure increasing from 0.484 to 0.59, while Eq. (38) gives a grid independent solution (GIDS) with the maximum pressure being stable at a value of 0.63. When increasing grid points to 4096 * 4096 for the GDS using Eq. (31), the maximum pressure is just close to that of the GIDS using Eq. (38). Therefore, Eq. (38) is more accurate and computationally inexpensive.

For the dynamic rolling contact problem, (see, Sec. 2.3.2), an analytical solution is not available. Instead, the numerical results are

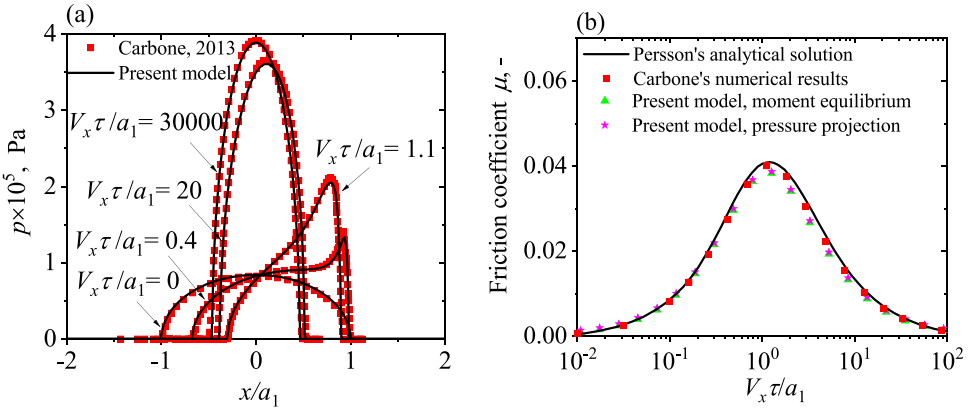

Fig. 10. Comparison of numerical results from the present model (lines) with those from Carbone and Putignano [26] at a wide range of rolling velocities: (a) pressure distribution (rolling to the right side), (b) friction coefficient.

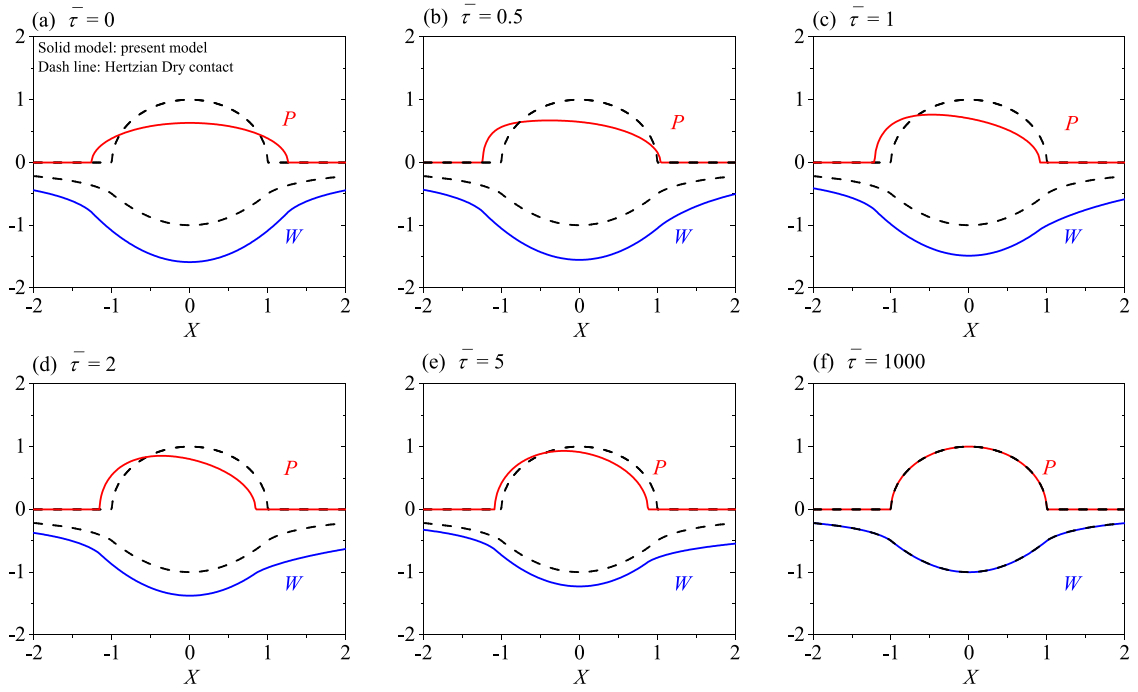

Fig. 11. Pressure and deformation distribution at different rolling velocities for a frictionless rolling contact between a rigid sphere and a viscoelastic half-space. The sphere is rolling forwards in the negative *x*-axis direction, and the corresponding Hertzian elastic solution of pressure and deformation with only the modulus E_f in the SLS model in reaction is drawn in dashed line for comparison. ($R_e = E_f/E_s = 1$).

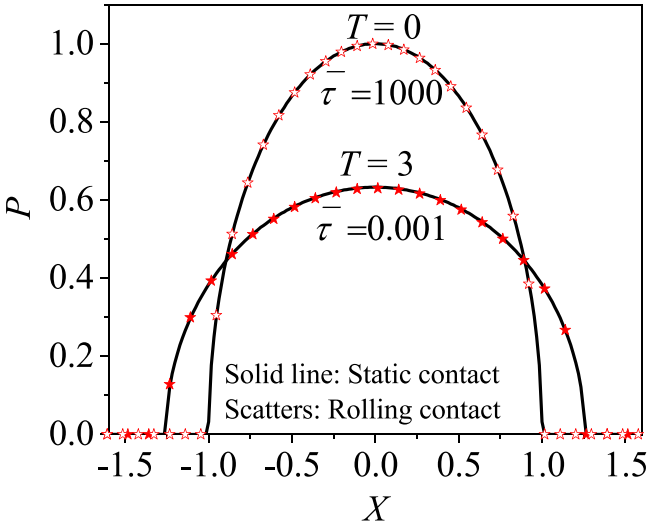

Fig. 12. Comparison of the pressure distribution between static and rolling viscoelastic contact at two extreme conditions when the responses are purely elastic: $T = 0$ and $T = 3(t = 3\tau)$ for static contact, $\bar{\tau} = 0.001$ and $\bar{\tau} = 1000$ for rolling contact. ($R_e = E_f/E_s = 1$).

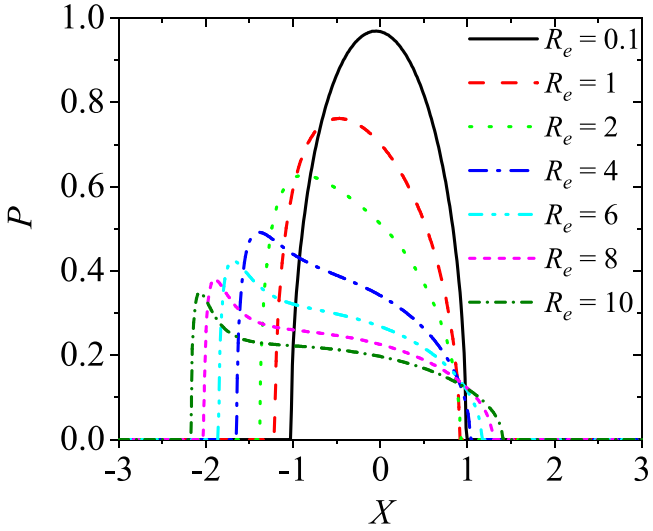

Fig. 13. Pressure distributions at different elasticity ratios for Deborah number $\bar{\tau} = 1$. (SLS viscoelastic model; the left side is the rolling entrance).

verified with numerical results obtained by Carbone and Putignano with a boundary element method [26], also using an SLS viscoelastic model. The operating conditions in [26] are $E_f = 10$ MPa, $E_f/E_0 = 10$ with E_0 the effective elastic modulus of the two springs in series at an extremely low velocity: $E_0 = 1/(1/E_s + 1/E_f)$, $R_0 = 10$ mm, $W_0 = 0.15$ N and $\tau = 0.01$ s. The dimensionless velocity $\bar{\tau}$ was varied over a wide range $0 \le \bar{\tau} \le 3 \times 10^4$, where a_1 is the Hertzian contact radius at an extremely low velocity with a modulus of E_0 [26,41]. Fig. 10 shows the centerline profiles of the results for pressure distribution for a range of rolling velocities, as well as the variation of the coefficient of friction with rolling velocity obtained using the two approaches indicated in Sec. 2.3.2, friction derived either by the moment equilibrium or by the pressure projection. The friction coefficients obtained using the present model were validated by comparing with Persson's [25] analytical solution and Carbone's [26] numerical results. Obviously the agreement is very good for both the pressure distribution and the friction coefficient in Fig. 10. In the remaining part of this section the speed dependent viscoelastic behavior that has been shown in Fig. 10 (a) is further analysed. In the dimensionless equations expressed in the coordinate system relative to the contact, the influence of the velocity in the integral transform kernel function (Green function) in Eq. (32) appears as in the dimensionless number $\bar{\tau} = \tau V_x/a_0$. The Deborah number is the ratio of two timescales, i.e. the material timescale which is the relaxation time τ and an exposure time during which a load acts, i.e. the exposure time in

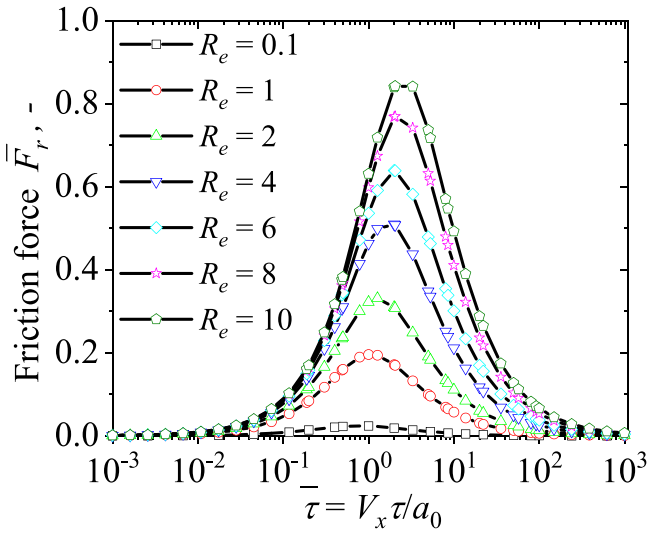

Fig. 14. Dimensionless friction force with different elasticity rations varied over Deoborah number, $\bar{\tau}$. (SLS viscoelastic model, calculated with moment equilibrium method, R_e values are the same as in Fig. 13).

the contact a_0/V_x. In this sense Fig. 10 (a) in fact shows results for different values of the Deborah number ranging from 0 to 30,000.

In Fig. 11 the centerline profiles of the dimensionless pressure P and the dimensionless deformation W are shown for the case of a smaller elasticity modulus ratio of $R_e = E_f/E_s = 1$, and values of the Deborah number ranging from 0 to 1000. Also shown in the figure as dashed line are the pressure and deformation for the reference case used for scaling, i.e. based on the modulus E_f in the SLS model.

At a very low or very high Deborah number the pressure distribution is Hertzian and thus symmetric (Fig. 11 (a) and (f)). These are the solutions characterized by the springs in the SLS model. At a low velocity, the dashpot does not play any role and the material behaves as a pure elastic material with a rigidity of E_0. At a high velocity, the dashpot does not have enough time to respond and becomes exceedingly rigid. The material response is then governed by the free spring of modulus, E_f. Hence, the deformation and pressure distribution in a rolling contact at the low and high extreme speed conditions are exactly the same as the solutions to the static contact problem at the time $T \to \infty$ and $T = 0$ respectively. This is illustrated in Fig. 12.

Solutions for other $\bar{\tau}$ (e.g., Fig. 11 (b)–(e)), show the transition between the two extreme cases. The pressure distributions are asymmetric, skewed towards the inlet side of the contact. The pressure becomes steeper in the inlet region compared to the low Deborah number Hertzian solution as the material behaves increasingly rigid when it enters the contact at a higher velocity. The contact area is shifted towards the entrance of the contact and there is a distinct difference between the front and the rear semi-length of the contact area, as reported in [26,29]. At the trailing edge of the contact, unlike elastic material of instantaneous response, the viscoelastic material needs more time to recover to its original state. These variations in pressure between the front and the rear of the contact lead to a rolling resistance (friction). With varying Deborah number (speed) the friction coefficient exhibits a bell shape as shown in Fig. 10 (b). The maximum friction coefficient occurs at a Deborah number close to $\bar{\tau} = 1$. Referring to the graphs in Fig. 11, this is the situation where the assymmetry in the pressure is the largest which coincides with the largest off center shift of the contact zone.

The effect of the elasticity ratio $R_e = E_f/E_s$ on the asymmetrical pressure distribution is shown in Fig. 13 for $\bar{\tau} = 1$. With increasing R_e the asymmetry increases as the contact edge moves further to the inlet side. The solution even has a local maximum close to the edge of the contact for $R_e = 6$, $R_e = 8$ and $R_e = 10$. These results imply that with increasing R_e in the numerical simulation the computational domain must be increased accordingly. This is also explained by the larger rigidity of the material entering the contact. As can be expected, the pressure peak in the inlet and the pressure asymmetry lead to a higher rolling resistance and a higher friction coefficient. This trend can be clearly seen from Fig. 14, which plots the variation of the dimensionless friction force with Deborah number at different elasticity ratios as used in Fig. 13.

4.3. Rolling/Sliding viscoelastic-on-viscoelastic contacts

So far the case of a rolling contact between a rigid ball and a viscoelastic half-space was considered. In this case, the rolling problem is equivalent to a frictionless sliding problem (rigid ball sliding on viscoelastic substrate) regarding the pressure distribution and surface deformation. This is similar to the behavior of an elastic contact, where

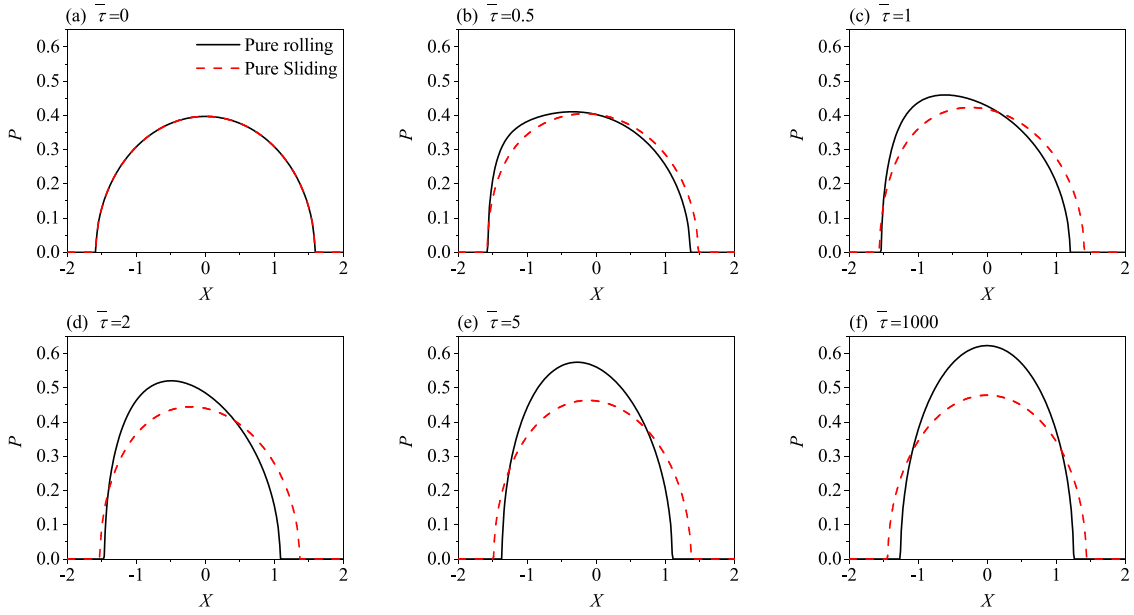

Fig. 15. Comparison of pressure distributions between rolling and sliding conditions for a viscoelastic contact with identical material of the two bodies. (SLS viscoelastic model with $R_e = E_f/E_s = 1$; the left side is the rolling/sliding entrance).

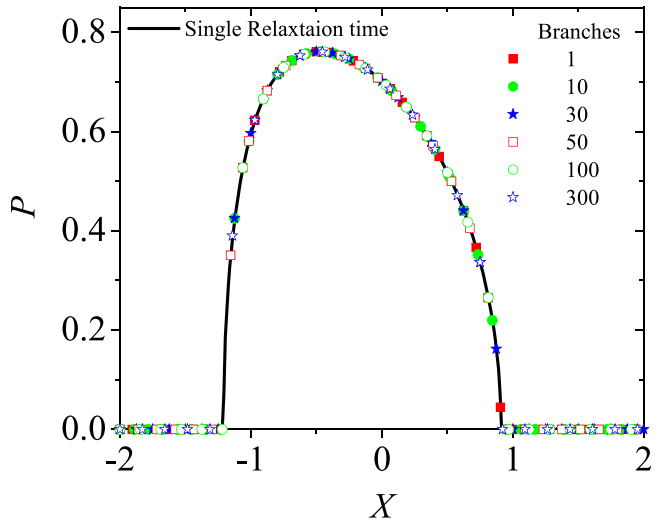

Fig. 16. Dimensionless pressure distribution along the central line of the contact for the multi-branch SLS model with different number of branches. (Deborah number $\bar{\tau} = 1$, $R_{e1} = R_{e2} = \cdots = R_{en} = 1$, where n is the number of branch.).

Table 1
Computational time for different number of branches of generalized SLS model to consider multi-relaxation times of viscoelastic materials. (Parameters: $R_e = E_{fi}/E_{si} = 1$, 512 *512 grid points and the computational domain is $8a_0$ in both x direction and y direction).

Number of branches, n	Computational time, s	Maximum pressure, -
1	72.9	0.76
10	73.4	0.76
30	78	0.76
50	90	0.76
100	96	0.76
300	161	0.76

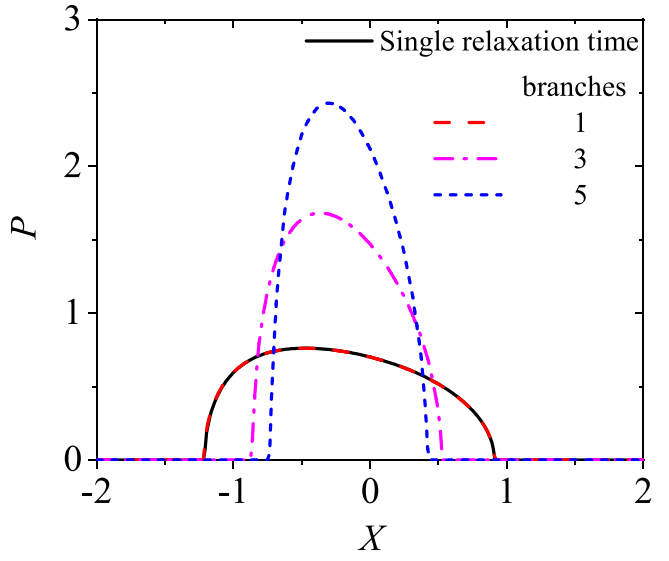

Fig. 17. Pressure distributions with different elasticity ratios and relaxation times on each branch for Deborah number $\bar{\tau} = 1$. (multi-branch SLS viscoelastic model with $R_{e1} = R_e$, $R_{e2} = 2R_e$, …, $R_{en} = nR_e$, and $\tau_1 = \tau$, $\tau_2 = 2\tau$, …, $\tau_n = n\tau$, where n is the number of branch.).

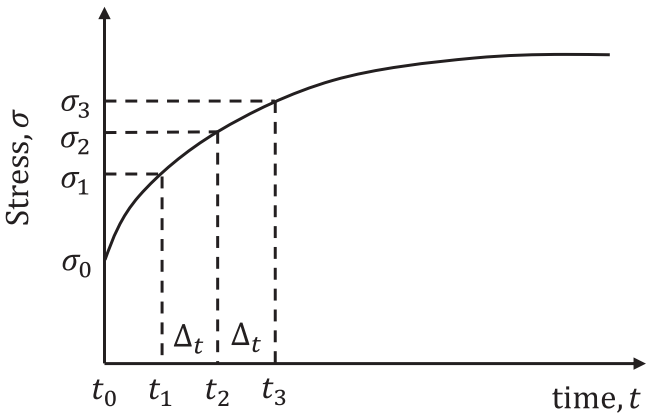

Fig. A1. Varying stress as input.

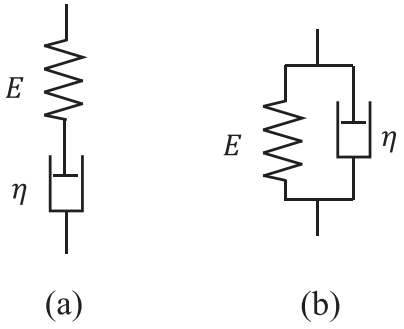

Fig. B1. 1D viscoelastic material models: (a) Maxwell model, (b) Kelvin-Voigt model.

in practice for the calculation of elastic deformation, an elastic-elastic contact is usually equivalent to a rigid-elastic contact by introducing a reduced elastic modulus. In this section we consider the case of two viscoelastic bodies. Because of the viscoelasticity of the material pure rolling and sliding are now fundamentally different. This effect is studied here by assuming that the two bodies are made of identical viscoelastic material and have identical mechanical properties.

For the pure rolling case, the two contact bodies have the same creep and deformation behavior, and the combined deformation can be obtained by summing up their individual contributions according to Eq. (38). While for the pure sliding case, only the moving body (the viecoelastic sphere or the viscoelastic half-space) shows the viscoelastic effect during the deformation process, the fixed one behaves elastically and deforms with a fixed modulus of E_0 as its speed is zero; this is also reported in [29]. Fig. 15 compares the calculated pressure distribution for these two cases at different speeds. At the lowest speed of $\bar{\tau} = 0$, the rolling case and the sliding case have identical pressure distribution since the two bodies show both elastic response of modulus E_0. As velocity increases, the pure rolling condition would bring more new material into the contact than the sliding contact with a surface in stationary. Therefore, pure rolling condition leads to a smaller contact radius and a larger contact pressure. At the highest speed of $\bar{\tau} = 1000$, the two bodies behave elastically in both the pure rolling case and the pure sling case, and the rigidity of the rolling contact (each body is characterized by a modulus of E_f) is larger than that of the sliding contact (one body is E_f, while the other is E_0). As a result, the final contact radius is smaller, and the maximum pressure is larger for the pure rolling case.

4.4. Multiple-relaxation times

Here, one example is given for viscoelastic materials of multiple

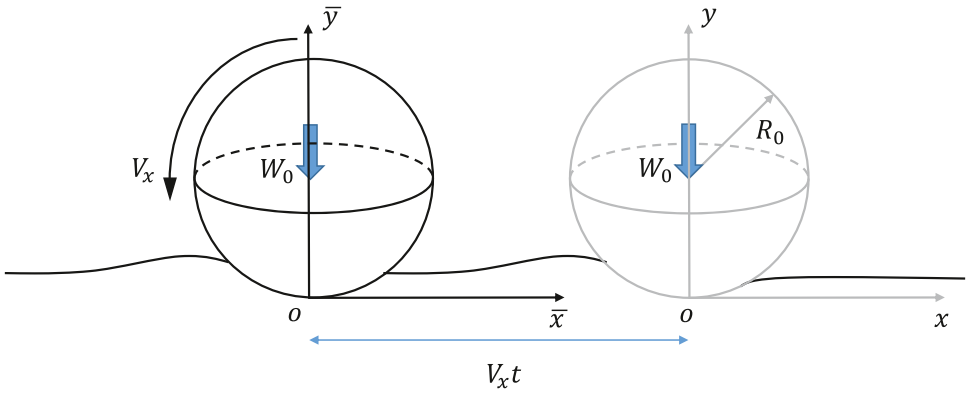

Fig. C1. Dynamic rolling contact problem formed between a rigid ball with a viscoelastic half-space (xoy: fixed coordinate system; $\bar{x}o\bar{y}$: moving coordinate system).

relaxation times to show the efficiency of the developed method by carrying out pressure calculation for a dynamic rolling contact problem described in Sec. 3.3. For the generalized SLS model, different number of branches n has been used, ranging from 1 to 300. To make the simulation results being comparable to one another, the effective viscoelastic properties of the material as a whole are set to be identical on purpose among different cases. This could be achieved by setting $E_{f1} = E_{f2} = \cdots = E_{fn} = E_f/n$, $E_{s1} = E_{s2} = \cdots = E_{sn} = E_s/n$, $R_{e1} = R_{e2} = \cdots = R_{en} = 1$ and $\tau_1 = \tau_2 = \cdots = \tau_n = \tau$. Fig. 16 shows identical pressure distributions along the central line of the contact for the multi-branch SLS model with different number of branches. Table 1 compares the computation time and the maximum contact pressure for different numbers of branches in the generalized SLS model using a laptop (CPU at 1.9 GHz). It can be found that with increasing numbers of branches, there is no significant increase in computational time, especially when the material can be described with less than 100 relaxation times.

Finally, another example of multi-branch SLS model is given for $\bar{\tau} = 1$ with different elastic ratio, $R_{en} = nR_e$, and relaxation times, $\tau_n = n\tau$, on each branch. In this case, the increase of branch numbers causes an increase in the rigidity of the viscoelastic material and thus leads to a higher pressure and a narrower contact width as shown in Fig. 17. The pressure distribution with $n = 1$ coincides with the pressure obtained with a single relaxation time, see Fig. 11 (c).

5. Conclusion

Several aspects of modeling and numerical simulation of viscoelastic point contact problems have been discussed in detail. Firstly, different ways to model the viscoelastic deformation were discussed for both static and rolling point contact problems. For the static problem the presented approach using the derivative of the creep compliance function of the material, Eq. (19), is most efficient. This approach was also used by Hooke and Huang [23] for the EHL dynamic rolling line contact problem. However, as it is sensitive to a low speed increased discretization error, for a rolling problem this approach is less suited, unless very fine grids can be used as is easily the case in a line contact. For the point contact an alternative approach is presented here. The viscoelastic deformation expression can be cast in an easy way to evaluate differential equation. This new equation, Eq. (38) allows accurate evaluation in an amount of computational time equivalent to that of the elastic deformation, also for complex models with multiple relaxation times. The methodology can be integrated straightforwardly in an existing contact solver, e.g. the Multigrid/Multilevel solution method presented in [34] which was used here.

Results have been presented for static and rolling dry point contacts. For the rigid indenter viscoelastic half-space static contact the results were validated with analytical solutions of Lee and Radok [13]. For the same configuration in rolling contact the results were compared with results from Carbone and Putignano [26], demonstrating the importance to use a sufficiently large domain. For this problem using the Standard Linear Solid (SLS) viscoelastic material model results of a parameter study are presented of variation of contact size, the pressure distribution. And the rolling friction has been analyzed over a wide range of values of the Deborah number. The condition where the assymetry in pressure is maximal is associated with the highest value of friction coefficient, which is around a value of unity of the Deborah number. Also the correlation between the static (creep) contact and the rolling contact solutions is shown, i.e. the initial (time $t = 0$) and the asymptotic ($t \to \infty$) solution for the static problem are identical to the high speed $V_x \to \infty$ and the $V_x = 0$ for the rolling contact problem. When considering two viscoelastic bodies in contact the viscoelasticity causes big differences between rolling and sliding running conditions of viscoelastic-to-viscoelastic contacts. Only one surface shows viscoelastic response and the other responses elastically under sliding condition, while the two moving surfaces response both viscoelastically in a pure rolling contact. This leads to differences in the pressure distribution and in the contact radius. Finally the approach proposed here is also shown to work for a multiple relaxation time problem. Future work will focus on point contact EHL problems between viscoelastic solids aimed at demonstrating exact scaling laws, experimental validation, and multi-island dry contact viscoelastic layer models mimicking EHL problems in mixed lubrication.

CRediT authorship contribution statement

Y Zhao: Conceptualization, Methodology, Software, Writing – original draft. **GE Morales-Espejel:** Supervision, Writing – review & editing. **CH Venner:** Conceptualization, Supervision, Writing – review & editing, Project administration.

Declaration of Competing Interest

The authors declare that they have no known competing financial interests or personal relationships that could have appeared to influence the work reported in this paper.

Acknowledgements

The authors would like to thank Mr. Bernie van Leeuwen, SKF Research and Technology Development Director, for his kind permission to publish this article. The authors would like to thank Dr. Ehret Pascal for sharing his knowledge on this topic and thank Dr. Binbin Zhang and Dr. Haichao Liu for proofreading. The authors would thank Dr. C.W. Visser for his helpful discussion and comments. The first author acknowledges the China Scholarship Council (CSC) for providing the PhD scholarship.

Appendix A. Stress Strain relation of viscoelastic material

Key element in the modeling of linear viscoelastic material behavior is the so-called correspondence principle proposed by Alfrey [9]. This implies that the viscoelastic solution to a problem can be derived from an appropriate elastic solution [8]. The stress-strain relationship is then expressed as:

$$\sigma(t) = \psi_r(t)\epsilon_0 \tag{A.1}$$

where $\psi_r(t)$ is the relaxation modulus function, which for a specific material can be determined from a relaxation test with a constant strain as input. Alternatively the behavior may be formulated in terms of the stain as:

$$\epsilon(t) = \varphi_c(t)\sigma_0 \tag{A.2}$$

where $\varphi_c(t)$ is the creep compliance function which for a specific material can be determined from a creep test with a constant stress as input. For specific models such as the Maxwell model, the Kelvin-Voigt model and the Standard Linear Solid model, the functions $\psi_r(t)$ and $\varphi_c(t)$ can easily be determined, see Appendix B.

Note that the derivation of creep compliance functions for the basic viscoelastic models uses a constant stress as input. While for a variable stress input as shown in Fig. A1 to linear viscoelastic materials, the strain output can be obtained by applying the Boltzmann superposition principle [8]. Its derivation is shown below.

(1) *Proportionality*: Firstly, representing the variable stress input by a series of step inputs, each of which begins at different time as shown in Fig. A1. Thus, the stress input can be expressed in the following form:

$$\sigma(t) = \sigma_0 + (\sigma_1 - \sigma_0) + (\sigma_2 - \sigma_1) + \cdots + (\sigma_n - \sigma_{n-1}) \tag{A.3}$$

At every time, the strain response is proportional to the amplitude of a constant stress step applied at $t = t_0$:

$$\epsilon_i(t) = \Delta\sigma_i\varphi_c(t - t_i) \tag{A.4}$$

(2) *Superposition*: The strain response to two subsequently (at time $t = t_0$ and $t = t_1$) applied constant amplitude ($\Delta\sigma_0$ and $\Delta\sigma_1$) stress steps equals the sum of the separate response. For $t > t_1$

$$\epsilon(t) = \Delta\sigma_0\varphi_c(t - t_0) + \Delta\sigma_1\varphi_c(t - t_1) \tag{A.5}$$

Every excitation can now be seen as an infinite sequence of infinitesimal small stress steps. Superposition then leads to the so-called Boltzmann Integrals. Assuming $t_0 = 0$ and taking the limit as n approaches infinity and Δ_t approaches zero, one obtains:

$$\epsilon(t) = \sigma_0\varphi_c(t) + \int_{0^+}^{t} \varphi_c(t - q)\frac{d\sigma(q)}{dq}dq \tag{A.6}$$

For relaxation test by using a varying strain as input, the stress output can be expressed as following,

$$\sigma(t) = \epsilon_0\psi_r(t) + \int_{0^+}^{t} \psi_r(t - q)\frac{d\epsilon(q)}{dq}dq \tag{A.7}$$

B. Creep compliance function

The creep compliance functions for some of the well known viscoelastic material model are derived below. Viscoelastic material behavior models describe the relation among stress σ, stress rate $\dot{\sigma}$, strain ϵ and strain rate $\dot{\epsilon}$. The models are usually 1D models consisting of elastic elements:

$$\sigma = E\epsilon \tag{B.1}$$

where E is the modulus of elasticity, and the dashpot elements characterized by:

$$\sigma = \eta\dot{\epsilon} \tag{B.2}$$

In the models spring and dashpot elements are combined either in series or in parallel so as to mimic a specific behavior. The number of elements ranges from two as in the Maxwell and Kelvin-Voigt model in Fig. B1, to three in the SLS models in Fig. 2, and even more, e.g. in Fig. 3 the multi-branch SLS model. Some of the most basic models are shown in Fig. B1. The creep compliance function for these models is derived below.

B.1. Maxwell Model

.Fig. B1 (a) schematically shows the Maxwell model consisting of a spring with stiffness E and dashpot with viscosity η. Let ϵ_1 be the strain of the spring part and ϵ_2 the strain associated with the dashpot. As the elements are in series by definition $\sigma = \sigma_1 = \sigma_2$, and

$$\epsilon = \epsilon_1 + \epsilon_2 = \frac{\sigma}{E} + \epsilon_2 \tag{B.3}$$

Differentiation with respect to time gives:

$$\dot{\epsilon} = \frac{\dot{\sigma}}{E} + \dot{\epsilon}_2 = \frac{\dot{\sigma}}{E} + \frac{\sigma}{\eta} \tag{B.4}$$

We can now write it in the so-called standard form, which is when the equation written with σ and $\dot{\sigma}$ on one side scaled such that σ appears with multiplication unity, and ϵ and $\dot{\epsilon}$ on the other side of the equality sign, one obtains:

$$\sigma + \eta \frac{\dot{\sigma}}{E} = \eta \dot{\epsilon} \tag{B.5}$$

To obtain the creep compliance function we apply a constant stress $\sigma(t) = \sigma_0$. In that case $\dot{\sigma} = 0$. The model equation then reduces to:

$$\sigma_0 = \eta \dot{\epsilon} \tag{B.6}$$

which can be solved for $\epsilon(t)$ giving

$$\epsilon(t) = \frac{\sigma_0}{\eta} t + C \tag{B.7}$$

where the integration constant C follows from the initial condition that $\epsilon(0) = \frac{\sigma_0}{E}$, so that:

$$\epsilon(t) = \frac{\sigma_0}{\eta} t + \frac{\sigma_0}{E} = \varphi_c(t)\sigma_0 \tag{B.8}$$

where $\varphi_c(t)$ is the creep compliance function. Obviously one finds:

$$\varphi_c(t) = \frac{t}{\eta} + \frac{1}{E} \tag{B.9}$$

B.2. Kelvin-Voigt model

In the Kelvin-Voigt model, Fig. B1(b), a spring element and a dashpot element are in parallel. Let ϵ_1 be the strain associated with the spring element and ϵ_2 the strain associated with the dashpot element. As the elements are in parallel the strain must be equal: $\epsilon = \epsilon_1 = \epsilon_2$. The total stress is the sum of the stresses $\sigma = \sigma_1 + \sigma_2$. We now seek the relation between σ, stress rate $\dot{\sigma}$, ϵ and $\dot{\epsilon}$.

$$\sigma = \sigma_1 + \sigma_2 = E\epsilon + \eta \dot{\epsilon} \tag{B.10}$$

To find the creep compliance function we apply a constant stress $\sigma(t) = \sigma_0$ with $\dot{\sigma} = 0$ giving:

$$\sigma_0 = E\epsilon + \eta \dot{\epsilon} \tag{B.11}$$

To get the creep compliance function we need to solve $\epsilon(t)$ from the inhomogenous ordinary differential equation:

$$E\epsilon + \eta \frac{d\epsilon}{dt} = \sigma_0 \tag{B.12}$$

This is done in two steps using standard methods. First we determine the solution ϵ_h of the homogeneous equation, and next find one particular solution of the inhomogeneous equation ϵ_p. The solution is $\epsilon(t) = \epsilon_h(t) + \epsilon_p(t)$.

$$E\epsilon + \eta \frac{d\epsilon}{dt} = 0 \tag{B.13}$$

Substitution of $\epsilon_h(t) = e^{\lambda t}$ gives $\lambda = -\frac{E}{\eta}$ so that the solution is

$$\epsilon_h(t) = Ce^{-\frac{E}{\eta}t} \tag{B.14}$$

Next, we easily see a particular solution of the inhomogeneous equation as $\epsilon_p(t) = \frac{\sigma_0}{E}$. So the solution $\epsilon(t)$ is:

$$\epsilon(t) = \frac{\sigma_0}{E} + Ce^{-\frac{E}{\eta}t} \tag{B.15}$$

The constant C follows the initial condition: $\epsilon(0) = 0$ as the response of the material to the applied constant stress is not immediate due to the dashpot and the spring in parallel. Substitution of $\epsilon(0) = 0$ in Eq. B.14 gives $C = -\frac{\sigma_0}{E}$. So that

$$\epsilon(t) = \frac{\sigma_0}{E} + Ce^{-\frac{E}{\eta}t} = \frac{\sigma_0}{E}(1 - e^{-\frac{t}{\frac{\eta}{E}}}) \tag{B.16}$$

The ratio η/E is referred to as the retardation time. From the definition $\epsilon(t) = \sigma_0\varphi_c(t)$, we find the creep compliance function for Kelvin-Voigt model:

$$\varphi_c(t) = \frac{1}{E}(1 - e^{-t/\frac{\eta}{E}}) \tag{B.17}$$

C. Viscoelastic deformation equation

For a contact of elastic materials, e.g. for a standard Hertzian dry contact, the deformation occurs instantaneously when an external load is applied. Therefore, a static contact and a frictionless rolling/sliding contact have identical governing equations as well as the same numerical solution under steady-state conditions. For a viscoelastic contact in this study, the time-dependent properties of the material have substantial effects on the process of surface deformation, such as the time-varying contact area for a static contact and the speed/frequency dependent deformation for a dynamic contact. Here shows the derivation process of the deformation equation from the elastic ones to the viscoelastic one for both static contact problem and pure rolling contact problem. For elastic contacts based on the semi-infinite half-space approximation and the linear elasticity assumption, the elastic Boussinesq double integral in Eq. (C.1) is widely adopted to determine the local normal displacement of the contact surfaces for homogeneous and isotropic solids [36], as

$$u_e(x,y) = \frac{1-\nu^2}{\pi E}\iint \frac{p(x',y')}{\sqrt{(x-x')^2+(y-y')^2}}\mathrm{d}x'\mathrm{d}y' \tag{C.1}$$

The benefit of using Eq. (C.1) is that the local elastic deformation of homogeneous and isotropic solids can be modelled and calculated in two dimensions (x and y directions) instead of fully solving the three-dimensional stress equilibrium equation, e.g. as the solution in Ref. [42].

C.1. Static contact problem

Like the derivation process of the stress-strain relationship for a stress variable input in Appendix A, for the normal deformation of isotropic viscoelastic contacts, the viscoelastic 'Boussinesq' equation can be formulated following the correspondence principle [10] and the solution proposed in [19]:

(1) Replacing the elastic compliance, $1/E$, with the creep compliance function, $\varphi_c(t)$, of the viscoelastic model in Eq. (C.1);.

(2) Decomposing the pressure history into infinite sequence of infinitesimal small pressure steps in the time domain;.

(3) Calculating the response of every pressure excitation, $\Delta p(p(x, y, t_n) - p(x, y, t_{n-1}))$, using viscoelastic 'Boussinesq' equation:

$$u_n(x,y) = \frac{1-\nu^2}{\pi}\varphi_c(t-t_n)\iint \frac{p(x',y',t_n)-p(x',y',t_{n-1})}{\sqrt{(x-x')^2+(y-y')^2}}\mathrm{d}x'\mathrm{d}y' \tag{C.2}$$

(4) Superposing all the contributions based on the linear viscoelasticity assumption. The deformation of viscoelastic material at time t can be obtained as

$$\begin{aligned} u(x,y,t) = {} & \frac{1-\nu^2}{\pi}\varphi_c(t)\iint \frac{p(x',y',0)}{\sqrt{(x-x')^2+(y-y')^2}}\mathrm{d}x'\mathrm{d}y' \\ & + \frac{1-\nu^2}{\pi}\int_{0^+}^{t}\varphi_c(t-q)\iint \frac{1}{\sqrt{(x-x')^2+(y-y')^2}}\frac{\partial p(x',y',q)}{\partial q}\mathrm{d}x'\mathrm{d}y'dq \end{aligned} \tag{C.3}$$

Compared with elastic deformation equation, Eq. (C.1), one more integration in the time dimension appears in order to take into account the effect of historical pressures on the deformation at all instants q. Changing the order of integration for the second term to the right side, Eq.(C.3) can be expressed as

$$\begin{aligned} u(x,y,t) = {} & \frac{1-\nu^2}{\pi}\varphi_c(t)\iint \frac{p(x',y',0)}{\sqrt{(x-x')^2+(y-y')^2}}\mathrm{d}x'\mathrm{d}y' \\ & + \frac{1-\nu^2}{\pi}\iint \frac{1}{\sqrt{(x-x')^2+(y-y')^2}}\int_{0^+}^{t}\varphi_c(t-q)\frac{\partial p(x',y',q)}{\partial q}dq\mathrm{d}x'\mathrm{d}y' \end{aligned} \tag{C.4}$$

Integrating by parts for the integral with respect to the time variable t in Eq. (C.4) as

$$\begin{aligned} \int_{0^+}^{t}\varphi_c(t-q)\frac{\partial p(x',y',q)}{\partial q}dq = {} & [\varphi_c(t-q)p(x',y',q)]|_{0^+}^{t} - \int_{0^+}^{t}p(x',y',q)d\varphi_c(t-q) \\ = {} & \varphi_c(0)p(x',y',t) - \varphi_c(t)p(x',y',0) - \int_{0^+}^{t}p(x',y',q)\frac{d\varphi_c(t-q)}{dq}dq \end{aligned} \tag{C.5}$$

Substituting Eq. (C.5) into Eq. (C.4), the viscoelastic deformation equation can be rephrased as

$$u(x,y,t) = \varphi_c(0)w_e(x,y,t) + \int_{0^+}^{t}\frac{d\varphi_c(q)}{dq}w_e(x,y,t-q)dq \tag{C.6}$$

where $w_e(x,y,t) = \frac{1-\nu^2}{\pi}\iint \frac{p(x',y',t)}{\sqrt{(x-x')^2+(y-y')^2}}\mathrm{d}x'\mathrm{d}y'$. Compared to Eq. 17, the local deformation at each instant now is expressed as the multiplication of the derivative of the creep compliance function and the corresponding 'elastic' deformation, $w_e(x, y, t)$.

C.2. Rolling contact problem

For the dynamic contact problem, a rigid sphere is rolling or sliding on a semi-infinite viscoelastic substrate with a constant speed, V_x, the deformation equation Eq.(C.6) could be simplified in the following way.

The *xoy* coordinate system is fixed on the substrate while the $\bar{x}o\bar{y}$ coordinate system moves with the rigid sphere, shown in Fig. C1.

The relationships between the fixed *xoy* and the moving $\bar{x}o\bar{y}$ coordinate systems are

$$\begin{aligned}\bar{x} &= x + V_x t\\ \bar{y} &= y\end{aligned} \tag{C.7}$$

Eq. (C.6) can be written as

$$\begin{aligned}u(x,y,t) &= \frac{1-\nu^2}{\pi}\varphi_c(0)\iint \frac{p(x',y',t)}{\sqrt{(x-x')^2+(y-y')^2}}\mathrm{d}x'\mathrm{d}y'\\ &+\frac{1-\nu^2}{\pi}\int_{0^+}^{t}\frac{d\varphi_c(q)}{dq}\iint \frac{p(x',y',t-q)}{\sqrt{(x-x')^2+(y-y')^2}}\mathrm{d}x'\mathrm{d}y'dq\end{aligned} \tag{C.8}$$

Restricting the analysis to be in steady state regime and using the relationships in Eq.(C.7), Eq.(C.8) can be represented in the moving coordinate, $\bar{x}o\bar{y}$, as

$$\begin{aligned}u(\bar{x},\bar{y}) &= \frac{1-\nu^2}{\pi}\varphi_c(0)\iint \frac{p(\bar{x}',\bar{y}')}{\sqrt{(\bar{x}-\bar{x}')^2+(\bar{y}-\bar{y}')^2}}\mathrm{d}\bar{x}'\mathrm{d}\bar{y}'\\ &+\frac{1-\nu^2}{\pi}\int_{0}^{\infty}\frac{d\varphi_c(q)}{dq}\iint \frac{p(\bar{x}'-V_xq,\bar{y}')}{\sqrt{(\bar{x}-\bar{x}')^2+(\bar{y}-\bar{y}')^2}}\mathrm{d}\bar{x}'\mathrm{d}\bar{y}'dq\end{aligned} \tag{C.9}$$

Define $s = \bar{x}' - V_xq$, Eq.(C.9) can be represented as

$$\begin{aligned}u(\bar{x},\bar{y}) &= \frac{1-\nu^2}{\pi}\varphi_c(0)\iint \frac{p(\bar{x}',\bar{y}')}{\sqrt{(\bar{x}-\bar{x}')^2+(\bar{y}-\bar{y}')^2}}\mathrm{d}\bar{x}'\mathrm{d}\bar{y}'\\ &+\frac{1-\nu^2}{\pi}\int_{0}^{\infty}\frac{d\varphi_c(q)}{dq}\iint \frac{p(s,\bar{y}')}{\sqrt{(\bar{x}-V_xq-s)^2+(\bar{y}-\bar{y}')^2}}ds\mathrm{d}\bar{y}'\end{aligned} \tag{C.10}$$

The double integral in the equation, $\iint \frac{p(\bar{x}',\bar{y}')}{\sqrt{(\bar{x}-\bar{x}')^2+(\bar{y}-\bar{y}')^2}}\mathrm{d}\bar{x}'\mathrm{d}\bar{y}'$, which means that the deformation at a local grid point, $(\bar{x},\bar{y})$, depends on the pressure distribution at all points, $(\bar{x}',\bar{y}')$, in the computational domain. Then, $p(\bar{x}',\bar{y}')$ and $p(s,\bar{y}')$ in Eq.(C.10) all indicate the pressures at different grid points in the computational domain, Eq.(C.10) can be rewritten in a standard form,

$$\begin{aligned}u(\bar{x},\bar{y}) &= \frac{1-\nu^2}{\pi}\varphi_c(0)\iint \frac{p(\bar{x}',\bar{y}')}{\sqrt{(\bar{x}-\bar{x}')^2+(\bar{y}-\bar{y}')^2}}\mathrm{d}\bar{x}'\mathrm{d}\bar{y}'\\ &+\frac{1-\nu^2}{\pi}\int_{0}^{\infty}\frac{d\varphi_c(q)}{dq}\iint \frac{p(\bar{x}',\bar{y}')}{\sqrt{(\bar{x}-V_xq-\bar{x}')^2+(\bar{y}-\bar{y}')^2}}\mathrm{d}\bar{x}'\mathrm{d}\bar{y}'\end{aligned} \tag{C.11}$$

Hunter [2] derived the same equation as Eq. (C.11) for viscoelastic deformation by using the Fourier transform method. A common target of these two derivation methods is to convert the viscoelastic deformation from a time domain to a space domain for rolling viscoelastic contact problems. As a result, the summation at different instants in the time domain in Eq. (C.3) or Eq. (C.6) is transformed into a summation of different grid points in the space domain in Eq. (C.11).

References

[1] v. Emden E, Venner CH, Morales-Espejel GE. Investigation into the viscoelastic behaviour of a thin lubricant layer in an ehl contact. Tribol Int 2017;111:197–210.

[2] Hunter SC. The rolling contact of a rigid cylinder with a viscoelastic half space. J Appl Mech 1961;28:611–7.

[3] Holmberg K, Erdemir A. Influence of tribology on global energy consumption, costs and emissions. Friction 2017;5:263–84.

[4] Damiens B, Venner CH, Cann PME, Lubrecht AA. Starved lubrication of elliptical ehd contacts. J Tribol 2004;126:105–11.

[5] Ahn BK, Lee DW, Israelachvili JN, Waite JH. Surface-initiated self-healing of polymers in aqueous media. Nat Mater 2014;13:867–72.

[6] Licup AJ, Munster S, Sharma A, Sheinman M, Jawerth LM, Fabry B, et al. Stress controls the mechanics of collagen networks. Proc Natl Acad Sci USA 2015;112:9573–8.

[7] Rus D, Tolley MT. Design, fabrication and control of soft robots. Nature 2015;521:467–75.

[8] Brinson HF, Brinson LC. Polymer engineering science and viscoelasticity: an introduction. Springer,; 2008.
[9] Alfrey T. Non-homogeneous stresses in visco-elastic media. Q Appl Math 1944;2:113–9.
[10] Christensen RM. Theory of viscoelasticity: an introduction. Elsevier,; 1982.
[11] Lee EH. Stress analysis in visco-elastic bodies. Q Appl Math 1955;13:183–90.
[12] Lee EH. Stress analysis in viscoelastic materials. J Appl Phys 1956;27:665–72.
[13] Lee EH, Radok JRM. The contact problem for viscoelastic bodies. J Appl Mech 1960;27:438–44.
[14] Hunter SC. The hertz problem for a rigid spherical indenter and a viscoelastic half-space. J Mech Phys Solids 1960;8:219–34.
[15] Ting TCT. The contact stresses between a rigid indenter and a viscoelastic half-space. J Appl Mech 1966;33:845–54.
[16] Graham GAC. The contact problem in the linear theory of viscoelasticity when the time dependent contact area has any number of maxima and minima. Int J Eng Sci 1967;5:495–514.
[17] Ting TCT. Contact problems in the linear theory of viscoelasticity. J Appl Mech 1968;35:248–54.
[18] Greenwood JA. Contact between an axisymmetric indenter and a viscoelastic half-space. Int J Mech Sci 2010;52:829–35.
[19] Chen WW, Wang QJ, Huan Z, Luo X. Semi-analytical viscoelastic contact modeling of polymer-based materials. J Tribol-Trans 2011;133.
[20] Koumi KE, Nelias D, Chaise T, Duval A. Modeling of the contact between a rigid indenter and a heterogeneous viscoelastic material. Mech Mater 2014;77:28–42.
[21] Goriacheva I. Contact problem of rolling of a viscoelastic cylinder on a base of the same material. J Appl Math Mech 1973;37:877–85.
[22] Panek C, Kalker JJ. Three-dimensional contact of a rigid roller traversing a viscoelastic half space. IMA J Appl Math 1980;26:299–313.
[23] Hooke CJ, Huang P. Elastohydrodynamic lubrication of soft viscoelastic materials in line contact. Proc Inst Mech Eng Part J-J Eng Tribol 1997;211:185–94.
[24] Aleksandrov VM, Goryacheva IG, Torskaya EV. Sliding contact of a smooth indenter and a viscoelastic half-space (3d problem). Dokl Phys 2010;55:77–80.
[25] Persson BN. Rolling friction for hard cylinder and sphere on viscoelastic solid. Eur Phys J E Soft Matter 2010;33:327–33.
[26] Carbone G, Putignano C. A novel methodology to predict sliding and rolling friction of viscoelastic materials: theory and experiments. J Mech Phys Solids 2013;61:1822–34.
[27] Koumi KE, Chaise T, Nelias D. Rolling contact of a rigid sphere/sliding of a spherical indenter upon a viscoelastic half-space containing an ellipsoidal inhomogeneity. J Mech Phys Solids 2015;80:1–25.
[28] Putignano C, Dini D. Soft matter lubrication: does solid viscoelasticity matter? ACS Appl Mater Interfaces 2017;9:42287–95.
[29] Putignano C. Soft lubrication: a generalized numerical methodology. J Mech Phys Solids 2020;134.
[30] Putignano C, Reddyhoff T, Carbone G, Dini D. Experimental investigation of viscoelastic rolling contacts: a comparison with theory. Tribology Lett 2013;51:105–13.
[31] Stanley HM, Kato T. An fft-based method for rough surface contact. J Tribology 1997;119:481–5.
[32] Liu SB, Wang Q, Liu G. A versatile method of discrete convolution and fft (dc-fft) for contact analyses. Wear 2000;243:101–11.
[33] Brandt A, Lubrecht AA. Multilevel matrix multiplication and fast solution of integral equations. J Comput Phys 1990;90:348–70.
[34] C., Venner, A.A., Lubrecht, Multi-level methods in lubrication., volume 37, Elsevier, 2000.
[35] Popov VL, Heß M, Willert E. Handbook of contact mechanics: exact solutions of axisymmetric contact problems. Springer Nature; 2019.
[36] Johnson KL. Contact mechanics. Cambridge university press,; 1985.
[37] Habchi W. Finite element modelling of elastohydrodynamic lubrication problems. Wiley Online Library,; 2018.
[38] Polonsky IA, Keer LM. A numerical method for solving rough contact problems based on the multi-level multi-summation and conjugate gradient techniques. Wear 1999;231:206–19.
[39] Wang Q, Sun LL, Zhang X, Liu SB, Zhu D. Fft-based methods for computational contact mechanics. Front Mech Eng 2020;6:61.
[40] Beatson R, Greengard L. A short course on fast multipole methods. Wavel Multilevel Methods elliptic PDEs 1997;1:1–37.
[41] Zhang X, Wang Q, He T. Transient and steady-state viscoelastic contact responses of layer-substrate systems with interfacial imperfections. J Mech Phys Solids 2020;145.
[42] Zhang BB, Boffy H, Venner CH. Multigrid solution of 2d and 3d stress fields in contact mechanics of anisotropic inhomogeneous materials. Tribol Int 2020;149:105636.